Eddy tracking from in situ and satellite observations

Zachary K. Erickson[1], Erik Fields[2], Leah Johnson[3], Andrew F. Thompson[4], Lilian A. Dove[4], Eric D'Asaro[3], David A. Siegel[2]

[1]NOAA Pacific Marine Environmental Laboratory, Seattle, WA, USA
[2]Earth Research Institute, University of California Santa Barbara, Santa Barbara, CA, USA
[3]Applied Physics Laboratory, University of Washington, Seattle, WA, USA
[4]Environmental Science and Engineering, California Institute of Technology, Pasadena, CA, USA

Key Points:

- Ship-based, autonomous, and remote sensing observations were combined to identify, characterize and track a coherent anticyclonic eddy
- Estimates of the eddy center and spatial extent derived from altimetry and in situ observations had similar accuracy
- Constant or smoothly varying sea level anomaly thresholds better represent eddy spatial extent than other satellite-based methods

Corresponding author: Zachary K. Erickson, zachary.k.erickson@noaa.gov

Abstract

Mesoscale eddies are a dominant source of spatial variability in the surface ocean and play a major role in the biological marine carbon cycle. Satellite altimetry is often used to locate and track eddies, but this approach is rarely validated against in situ observations. Here we compare measurements of a small (under 25 km radius) mode water anticyclonic eddy over the Procupine Abyssal Plain using CTD and ADCP measurements from 3 ships, 2 gliders, 2 profiling floats, and one Lagrangian float with those derived from sea level anomaly. In situ estimates of the eddy center were estimated from maps of the thickness of its central isopycnal layer, from ADCP velocities at a reference layer, and from the trajectory of the Lagrangian float. These were compared to three methods using altimetric SLA: one based on maximizing geostrophic rotation, one based on a constant SLA contour, and one which maximizes geostrophic velocity speed along the eddy boundary. All algorithms were used to select CTD profiles that were within the eddy. The in-situ metrics agreed to 97%. The altimetry metrics showed only a small loss of accuracy, giving $> 90\%$ agreement with the in situ results. This suggests that current satellite altimetry is adequate for understanding the spatial representation of even relatively small mesoscale eddies.

Plain Language Summary

Rotating water masses called eddies are ubiquitous features in the ocean and are important because they can transport nutrients and heat and are often associated with enhanced biological activity. Eddies are accompanied by sea level anomalies (SLA), in the same way that atmospheric weather systems are associated with high or low pressure systems, and can therefore be observed and monitored by satellite altimeters. However, observations of SLA from satellite are relatively coarse compared with the spatial scales of eddies, and satellite-based algorithms are rarely rigorously tested against "ground truth" observations. We use data from a dense network of observations in the vicinity of a relatively small eddy in the North Atlantic Ocean to track this eddy for several weeks from direct ocean measurements and satellite algorithms. We find widespread agreement between the in situ metrics and the satellite altimetry results, suggesting that satellite-based eddy tracking is sufficient to track even eddies that are relatively small compared with the resolution of SLA products.

1 Introduction

Upper ocean circulation is dominated by mesoscale eddies, coherent structures with scales of 10–200 km that have the ability to trap and retain water masses at their cores (Richardson, 1993; Goni & Johns, 2001; Chelton et al., 2007, 2011; Abernathey & Haller, 2018). Primary productivity and biogeochemical cycling in the upper ocean is impacted by these eddies primarily through injection of nutrients into the euphotic zone due to uplift of interior isopycnals (Falkowski et al., 1991; Siegel et al., 1999; A. Martin & Pondaven, 2003), enhanced vertical velocities caused by along-isopycnal motion through sloping isopycnals (Freilich & Mahadevan, 2019), and submesoscale instabilities, which can also lead to enhanced carbon export through small-scale subduction (Brannigan, 2016; Brannigan et al., 2017; Whitt et al., 2019; Archer et al., 2020; Jing et al., 2021). The "trapping" properties of mesoscale eddies make them natural laboratories to study the growth, evolution, demise, and export of carbon from phytoplankton blooms (e.g. Heywood & Priddle, 1987; Ellwood et al., 2020).

Studies that consider the evolution of a phytoplankton bloom in an Eulerian reference frame must deconvolve variability associated with horizontal advection from biological changes, which can make interpretation challenging (Dickey et al., 1991; Erickson & Thompson, 2018; Bol et al., 2018; Estapa et al., 2019). This is especially impor-

tant for stationary time series such as moorings that convolve spatial and temporal variability. Even studies that are intended to be Lagrangian can run into difficulties when assets are initially placed in an area with high variability. For example, a significant part of the North Atlantic Bloom experiment in 2008 was challenging to interpret because of the advection of the reference frame through an eddy (Alkire et al., 2012), and the spreading of drifting instruments leads to difficulty in constraining water mass budgets. When the goal is to study the evolution of a phytoplankton bloom within a Lagrangian water mass, a good option is to site the measurements within a retentive feature such as a mesoscale eddy.

Mesoscale eddies (hereafter, "eddies") in the ocean are associated with a sea level anomaly (SLA) and can therefore be studied using satellite altimetry (Chelton et al., 2007, 2011). Algorithms to track these eddies typically involve detecting and following contours of SLA (Chelton et al., 2011), geostrophic velocities calculated from first derivatives of SLA (Mason et al., 2014), or strain, shear, and vorticity terms calculated from higher-order SLA derivatives (Isern-Fontanet et al., 2003). These algorithms allow eddies to be tracked over their entire lifetime, and their temporally changing properties, such as size and eccentricity, to be studied. However, few satellite-based eddy tracking studies also include hydrographic information. Isern-Fontanet et al. (2004) found that altimetry-based metrics of the size of eddies in the Algerian Basin agreed well with the size of the same eddies using data from hydrographic transects, but that the boundaries of the eddies were difficult to accurately determine from satellite. Chaigneau and Pizarro (2005) similarly found good agreement between sea level height from satellite and derived from opportunistic in situ hydrographic measurements from a WOCE [World Ocean Circulation Experiment] cruise; however, the coarse station spacing of the cruise, of about 56 km, limited the ability of this study to precisely locate the eddy boundary from either method.

The EXPORTS (EXport Processes in the Ocean from Remote Sensing) program was conducted in the North Atlantic (EXPORTS-NA) near the Porcupine Abyssal Plain (PAP) Sustained Observatory (Hartman et al., 2012) in May of 2021 (Figure 1A; Johnson et al. (in prep.)). The goal of EXPORTS-NA was to survey biological properties during the demise of the North Atlantic spring bloom and to assess the major export flux pathways connecting the upper layers with the ocean interior (Siegel et al., 2016). The PAP region has high horizontal variability, with significant variation in water properties on small (<10 km) spatial scales (Damerell et al., 2016; Erickson et al., 2020; Johnson et al., in prep.). Tracking of sinking particulates in a model suggests that particles at 3000 m depth are sourced from up to 140 km away, with high interannual variability driven by changing currents and mesoscale variability (Frigstad et al., 2015). The scientific need to conduct field sampling in a Lagrangian reference frame, as well as the reality of managing and maximizing the science returns of over 40 drifting assets used as part of the EXPORTS-NA deployment, required locating the experiment in a retentive feature, such as an eddy (e.g. d'Ovidio et al., 2013; Della Penna & Gaube, 2019).

In the lead-up to EXPORTS-NA, a system of satellite and glider-based analyses was used to locate a retentive eddy in which to conduct the experiment (Erickson et al., 2022). A series of modeled particle release experiments, using satellite-derived geostrophic velocities, were conducted to test the retentiveness of eddies. Particle trajectories starting within eddies were tracked both forwards and backwards in time to determine the retentiveness of the eddy, defined as the average longevity of the particles within each eddy. This method, along with other characteristics such as size and shape, was used to determine four target eddies within the PAP region, which were then sampled by three gliders deployed in April 2021, one month before EXPORTS-NA. The eddy that was chosen was a relatively small and circular anticyclonic mode water eddy, with a radius of approximately 25 km and maximum edge velocities of about 20 cm s^{-1} (Erickson et al., 2022).

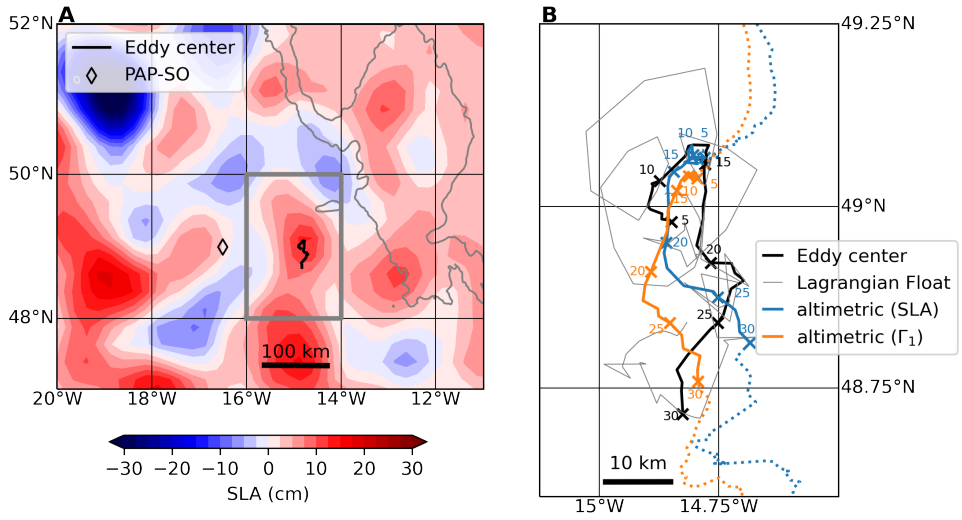

Figure 1. (A) Sea level anomaly (SLA) of the North Atlantic at the start of EXPORTS-NA, on 5 May 2021. Gray contours show the 1 and 3 km isobaths, and the gray box (16–14°W and 48–50°N) is the area shown in Figures 6 and 7 below. The trajectory of the eddy using in situ measurements (see text) is shown in black and is also in (B), where the blue and orange lines give the trajectory of the eddy using satellite methods and the light grey line is the path of the Lagrangian float. Numbers in (B) indicate the day in May (5–30 shown) and correspond with the 'x's every five days. Dotted colored lines in (B) extend the eddy center time series backwards (to the north) and forwards (to the south) in time beyond the EXPORTS-NA deployment. PAP-SO = Porcupine Abyssal Plain - Sustained Observatory.

The SLA anomaly associated with this eddy was smaller in magnitude than other nearby eddies (Figure 1A). Mode water eddies are characterized by a sub-surface region of low stratification (the "mode water"), resulting in a depression of isopycnals beneath the weakly stratified region and a shoaling of isopycnals above (McGillicuddy Jr, 2015). Geostrophic velocities at depth are anticyclonic and are primarily set by the slope of the deep isopycnals, typically representing the permanent pycnocline. Above the mode water layer, the doming of lighter isopycnals, typically representing the seasonal pycnocline, leads to a cyclonic shear in the geostrophic velocities that reduces the magnitude of the horizontal velocity associated with the eddy, suggesting that the sub-surface core of a mode water eddy is stronger than that of its near-surface waters. A consequence of the doming of these lighter isopycnals is that the SLA associated with a mode water eddy is reduced in comparison to non-mode water anticyclonic eddies of comparable strength.

Field observations of biological processes over time benefit from the knowledge of which measurements are associated with waters retained within the core of the eddy, as opposed to those in an environment exposed to injection of other water masses and, potentially, outside fluxes of nutrients or biomass (Johnson et al., in prep.). This paper introduces different metrics for in situ data to estimate whether a given measurement is taken from within or outside of the physically retentive core of the eddy. These metrics included distance from the eddy center and physical quantities derived from temperature and salinity. Satellite-based metrics using SLA and geostrophic velocities are also

Table 1. Platform profiles. Number of profiles are those that are located within the dashed box shown in Figure 1A and were made during the main part of the deployment (5–30 May, 2021). Deep profiles are those that extend to a potential density of at least 27.12 kg m^{-3}. SL = Slocum. SG = Seaglider. BGC = Biogeochemical float.

Platform	# profiles	# deep	# within eddy	# outside eddy
RSS James Cook	67	27	27	0
RSS Discovery	109	18	12	6
R/V Sarmiento de Gamboa	10	8	7	1
SL 305	285	259	112	147
SG 219	311	291	287	4
BGC 1902303	15	15	0	15
BGC 1902304	26	26	26	0
All	823	644	491	173

used to diagnose how well remote sensing products can predict whether a platform is inside or outside an eddy. While centered on one particular anticyclonic eddy in the North Atlantic, these methods can be applied to future field campaigns that are also targeting measurements following a Lagrangian trajectory.

2 Data

Three vessels collected observations within and around the target eddy during EXPORTS-NA (Table 1). The *RSS James Cook* tracked the evolution of eddy core water properties and fluxes, and remained primarily within the eddy. The *RSS Discovery* surveyed both within and outside the eddy to provide spatiotemporal context. The *R/V Sarmiento de Gamboa* was part of a different project measuring carbon flows and ecological distributions from the surface into the twilight zone but coordinated profiles with the EXPORTS-NA assets. Autonomous platforms were also deployed before and during EXPORTS-NA, including three gliders (SL305, SG219, and SG237) that scouted the region to find a suitable eddy in April of 2021 (Erickson et al., 2022), a Lagrangian float (D'Asaro, 2003) that was deployed near the center of the eddy at the beginning of the field deployment, two BGC floats (Claustre et al., 2020) initially deployed outside of (WMO ID 1902303) and within (WMO ID 1902303) the eddy, and over 40 drifting platforms, primarily surface drifters, that are not considered here.

Temperature and salinity data from each of these platforms were inter-calibrated against nearby profiles from the *RSS Discovery*, revealing temperature offset adjustments of 0.001–0.01°C and salinity adjustments of 0.001–0.01 PSU (Thompson, 2022). No time or pressure dependence was noted in any of the comparisons. The conductivity sensor on SG237 developed uncorrectable issues early in its deployment and is not used here. For the remainder of this paper, temperature and practical salinity from these platforms have been converted (Wright et al., 2011) into conservative temperature (Θ, °C) and absolute salinity (S_A, g kg^{-1}). These profiles are smoothed with a Gaussian window with a 5 m standard deviation and then used to calculate potential density (σ_0) and spice, the variation in Θ and S_A that does not contribute to variation in σ_0 (McDougall & Krzysik, 2015). Both potential density and spice are referenced to 0 db.

A subset of available profiles was used, including only profiles taken during the main part of the EXPORTS-NA deployment (5–30 May) near the eddy (within 14–16°W and 48–50°N, see gray box in Figure 1A) that profiled to densities of at least 27.2 kg m^{-3}, or approximately 600 m. This sub-selection of data was necessary to allow all eddy metrics, defined below, to be utilized, and to not include data from profiles within other nearby

eddies. From an initial 823 profiles (not including SG237 or profiling instruments such as the Lagrangian float that never reached the 27.2 kg m^{-3} isopycnal) this sub-selection process resulted in 644 "deep" profiles (Table 1).

Horizontal velocities were also used (Section 3.1) to define and track the eddy. Each ship was equipped with a narrow beam ADCP [Acoustic Doppler Current Profiler] measuring current velocities using acoustic signals at 75 and 150 kHz. ADCP-derived velocities were processed using the University of Hawaii Data Acquisition System (UHDAS) to a gridded data product at 5 minute resolution, with valid data down to about 400 m at 75 kHz and 150 m at 150 kHz. Only small differences were observed between the 75 and 150 kHz instruments, and the 150 kHz is used here. ADCP-derived horizontal velocities can be unreliable near the surface because of noise from bubbles injected under the ship's hull (Firing & Hummon, 2010) and at depth because of insufficient signal strength. 130 m was found to be a convenient trade-off between these two effects (not shown). ADCP data were only used while the ship was in motion, using a threshold speed of 0.5 m s^{-1}, or roughly 1 knot.

Finally, satellite altimeters provided SLA data, which are optimally interpolated onto a daily, 1/4° gridded product using spatial scales of 100–200 km and temporal scales of 10–45 days (Pujol et al., 2016). Ballarotta et al. (2019) estimate an effective spatial resolution in the study region of about 150–200 km. For comparison with a common eddy detection algorithm described below, a filtered SLA product was also calculated, SLA_{filt}, to remove larger-scale variability in the data. This filtered product is constructed by removing the large-scale SLA signature, estimated by filtering the SLA through a two-dimensional first-order Lancoz filter with a half maximum of 700 km.

3 Eddy detection methods

Eddies are typically defined as rotating volumes of water that are distinct from their surrounding environments. Horizontal velocities around the eddy are associated with horizontal gradients of SLA. Each of these properties—rotational velocities, SLA, horizontal interior density gradients, and a distinct water mass—can be used as a metric to understand the location, spatial extent, and strength of an eddy.

3.1 Rotational metrics

Horizontal velocities surrounding an eddy center will be predominantly tangential to the eddy center, rather than in a radial direction. Graftieaux et al. (2001) describe a method for determining the location of an eddy center from horizontal velocity measurements by calculating the local rotational metric $\Gamma_1(\mathbf{x})$, where $\mathbf{x} = (x, y)$ is a geographical location surrounded by horizontal velocity measurements $\mathbf{u}(\mathbf{x_i})$ (where $\mathbf{u} = (u, v)$) at locations $\mathbf{x_i}$ within a given radius of $\mathbf{x}$, here chosen as 40 km. Here two-dimensional (horizontal) vectors are denoted in bold-face text. $\Gamma_1(\mathbf{x})$ is calculated as

$$\Gamma_1(\mathbf{x}) = < \sin\theta >, \tag{1a}$$

$$\sin\theta = \frac{\mathbf{r} \wedge \mathbf{u}}{|\mathbf{r}| \cdot |\mathbf{u}|} = \frac{v \cdot \delta x - u \cdot \delta y}{(u^2 + v^2)^{1/2}(\delta x^2 + \delta y^2)^{1/2}}, \tag{1b}$$

where $< \cdot >$ represents a spatial average and θ are angles between $\mathbf{u}(\mathbf{x_i})$ and the positional vector $\mathbf{r} = (\mathbf{x_i} - \mathbf{x})$. $\Gamma_1(\mathbf{x})$ is unitless and varies between -1, denoting measurements that are purely tangential in an anticyclonic direction, and 1, representing tangential flow in a cyclonic direction. Fronts, by contrast, would result in a roughly uniform distribution of θ and therefore a $\Gamma_1(\mathbf{x})$ near 0. An eddy center is therefore determined as the location with maximum $|\Gamma_1(\mathbf{x})|$; that is, the area where the horizontal velocity measurements within a 40 km radius are most uniformly tangential/rotational.

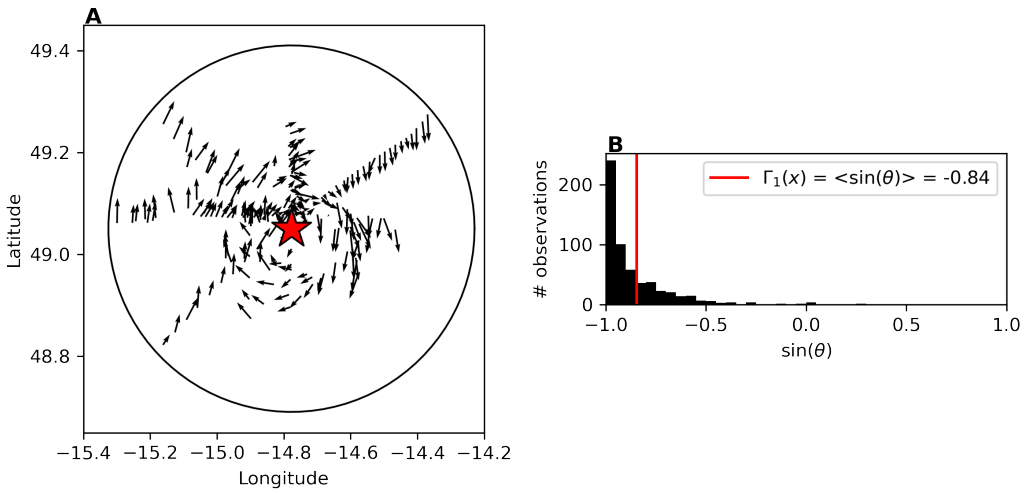

Figure 2. Example of calculating $\Gamma_1(\mathbf{x})$ from in situ ADCP velocity measurements (see Eq. 1. (A) ADCP velocities within 40 km (circle) of the calculated center position ($\mathbf{x}$, red star). (B) Histogram of $\sin(\theta)$ about the center, with a red vertical line showing the average value, $\Gamma_1(\mathbf{x})$.

Advection of an eddy can substantially reduce the magnitude of $\Gamma_1(\mathbf{x})$ within an eddy when the advection speed becomes comparable to the eddy's rotational speed. The local rotational metric $\Gamma_2(\mathbf{x})$, calculated similarly to $\Gamma_1(\mathbf{x})$ but with the mean horizontal velocities $\mathbf{u}_m =< \mathbf{u} >$ subtracted, corrects for the influence of eddy advection:

$$\Gamma_2(\mathbf{x}) =< \sin\theta_m >, \tag{2a}$$

$$\sin\theta_m = \frac{\mathbf{r} \wedge (\mathbf{u} - \mathbf{u_m})}{|\mathbf{r}| \cdot |\mathbf{u} - \mathbf{u_m}|} = \frac{(v - v_m) \cdot \delta x - (u - u_m) \cdot \delta y}{((u - u_m)^2 + (v - v_m)^2)^{1/2} (\delta x^2 + \delta y^2)^{1/2}}. \tag{2b}$$

Graftieaux et al. (2001) show that waters with $|\Gamma_2(\mathbf{x})| > 2/\pi$ are influenced primarily by rotation and can therefore be considered within the confines of an eddy. This suggests $|\Gamma_2(\mathbf{x})| = 2/\pi \approx 0.64$ as an appropriate threshold for the boundary of an eddy.

Horizontal velocities derived from ADCPs mounted on the *RSS James Cook* and *RSS Discovery* were used to calculate $\Gamma_1(\mathbf{x})$ using a moving time window of ± 2 days (see Figure 2). The location of minimum $\Gamma_1(\mathbf{x})$ is calculated every 12 hours and defined as the eddy center (Figure 1). Satellite-based measurements were calculated similarly every day from gridded 1/4° maps of geostrophic horizontal velocities. At 49°N this horizontal resolution, of 18 km in longitude and 28 km in latitude, corresponds to a low number of velocity "observations" surrounding any given $\mathbf{x}$. The data were therefore interpolated using a cubic spline to 1/40° resolution for the calculation of $\Gamma_{1,2}(\mathbf{x})$.

3.2 Sea surface height metrics

Anticyclonic eddies are associated with positive SLA on the order of tens of centimeters. Remote sensing of oceanic eddies from constellations of orbiting altimeters have built up a census of eddy properties and statistics throughout the global ocean over the past decades (Chelton et al., 2007, 2011; Faghmous et al., 2015). These approaches involve detecting peaks (or valleys, for cyclones) in SLA and defining a SLA contour about each peak that properly defines the boundary of the eddy.

Here we extend the Γ_2 approach above to define a matching SLA contour that has the most overlap with the effective eddy boundary Γ_2 contour of $-2/\pi$. This proposed

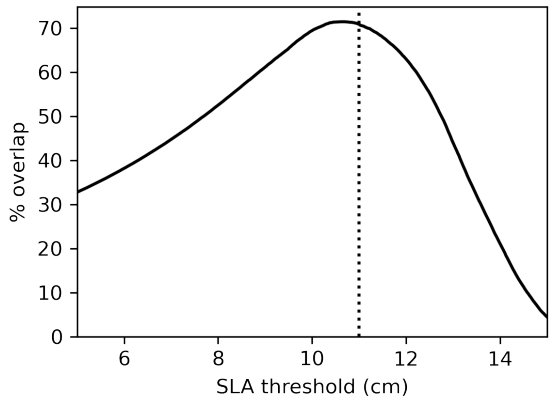

Figure 3. Percent overlap between Γ_2 and SLA thresholds, calculated as the areal ratio where both $\Gamma_2 < -2/\pi$ and SLA>$\text{SLA}_{\text{thres}}$, over a region where either $\Gamma_2 < -2/\pi$ or SLA>$\text{SLA}_{\text{thres}}$.

contour for Γ_2, however, occasionally conjoins with other nearby eddies to form highly irregular eddy boundaries. Therefore, only $\Gamma_2 = -2/\pi$ contours with a circularity of at least 0.7 were used to define the appropriate SLA contour, where the circularity is defined as the fraction of the given area that falls within a perfect circle with the same area. Using this approach, the SLA contour best defining the eddy was 11.0 cm (Figure 3).

Other approaches incorporate horizontal gradients in SLA, or geostrophic velocities, into the eddy boundary definition. The Mean Eddy Trajectory Analysis (currently version 3.2; META3.2) is used as a comparison here (Mason et al., 2014). This approach first looks for the largest area, or the SLA_{filt} contour with the smallest magnitude, about each SLA_{filt} peak with a circularity of at least 0.55 and containing only one local SLA_{filt} maximum or minimum, while requiring an area of between 8 and 1000 pixels (at $1/4° \times 1/4°$ resolution) and a SLA_{filt} amplitude of at least 1 cm, as the outermost extent of the eddy. It then estimates the SLA_{filt} boundary best representing the eddy itself as the contour within this area that maximizes the average geostrophic velocity along the eddy boundary, or equivalently is the SLA_{filt} contour that is associated with the largest horizontal SLA gradient (Mason et al., 2014; Pegliasco et al., 2022).

A number of other metrics are not considered here, but also rely on the relevant dominance of rotation about the eddy center. The Okubo-Weiss method (Isern-Fontanet et al., 2003), which measures the difference between rotational flow and shear/strain, is commonly used to determine eddies from altimetry. However, this method, which relies on multiple derivatives of SLA, is generally coarsely resolved when using 1/4° data. At the scale of the EXPORTS-NA eddy, this method predictably gave poor results (not shown). Another method, the Lagrangian-averaged vorticity deviation approach, advects particles along (geostrophic) velocities and calculates their individual vorticities, defining an eddy as a region where individual Lagrangian particles show high levels of vorticity (Haller et al., 2016). This method is essentially a Lagrangian version of the Eulerian Γ_2 method, but is considerably more computationally expensive to calculate.

3.3 Seawater property metrics

Glider SL305 was used to map waters within and outside of the target eddy and is therefore an ideal platform to construct a definition of interior water properties associated with distinct core eddy waters. Potential densities from SL305 indicate shoaling of waters near the eddy center lighter than about 27.15 kg m^{-3} when the platform was

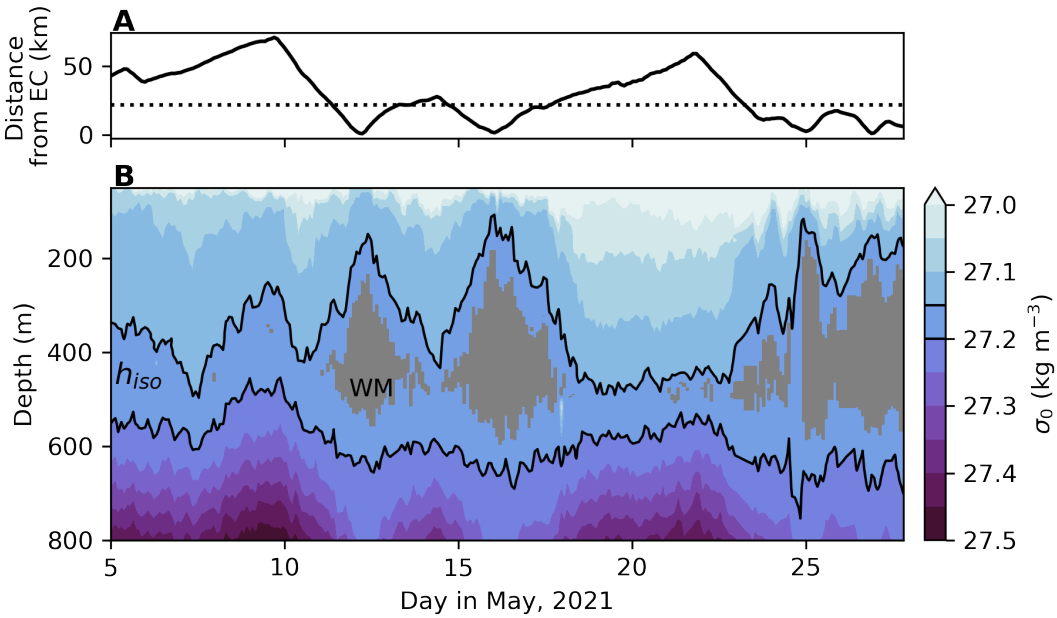

Figure 4. Data from ocean glider SL305 during EXPORTS-NA. (A) Distance from SL305 to the eddy center, with 22 km marked. (B) Potential density σ_0, with isopycnals involved in the calculation of h_{iso} (27.15 and 27.2 kg m^{-3}) in black. Gray filled region within h_{iso} denotes core WM, with σ_0 between 27.16–27.18 kg m^{-3} and spice between 1.74–1.76 kg m^{-3}.

near the eddy center, whereas isopycnals greater than about 27.2 kg m^{-3} deepen, creating the signature widening of interior isopycnal layers characteristic of an anticyclonic mode water eddy (Figure 4). The thickness, or height, of the core isopycnal layer 27.15–27.2 kg m^{-3}, h_{iso}, can therefore be used as a metric for the eddy extent.

Water mass characteristics can also define waters that are retained within the eddy. Temperature and salinity are relatively homogeneous at densities of about 27.17 kg m^{-3} for those profiles with h_{iso} greater than 275 m (Figure 5), suggesting that water mass (WM) properties with Θ of about 1.83°C and S_A near 35.63 g kg^{-1} designates that profile as passing through the interior eddy core. Potential density and spice thresholds were found to more precisely define these waters, and here we define the amount of core WM in each profile as the integral of waters with potential density from 27.16–27.18 kg m^{-3} and spice from 1.74–1.76 kg m^{-3} (gray area in Figure 4b; see also Johnson et al. (in prep.)).

3.4 Validation

The core isopycnal layer thickness was defined as the reference metric defining the eddy core, with profiles having a core thickness of over 275 m assumed to be within the eddy ($n = 491$), and outside of the eddy otherwise ($n = 173$; Table 1). Then, each method described above, along with the distance from the eddy center is calculated and given a threshold value. The results present the number of true positive and true negative predictions, where a given metric correctly diagnosed a profile as being within and outside of the eddy, respectively, and the number of false positive and false negative predictions, where the metric incorrectly diagnosed a profile as being within or outside of the eddy, respectively.

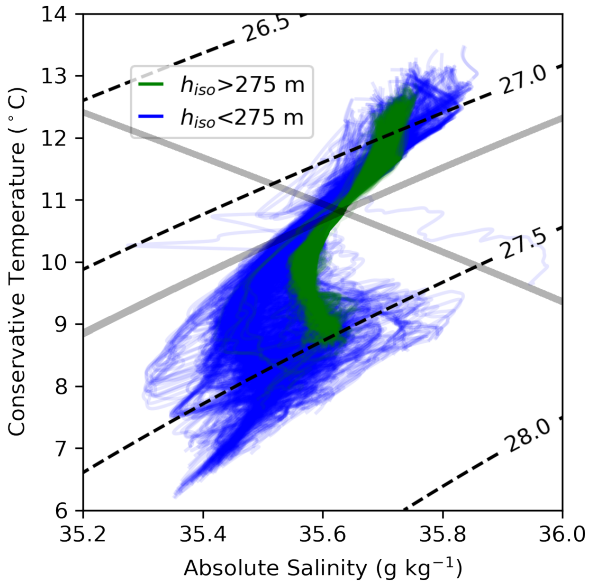

Figure 5. Profiles of S_A and Θ for profiles within (green) and outside (blue) the eddy, determined by a h_{iso} threshold of 275 m. Black dashed contours show potential density. Grey lines show values used to define core waters, with potential density from 27.16–27.18 kg m^{-3} and spice from 1.74–1.76 kg m^{-3}.

4 Results

4.1 Eddy center

Calculation of $\Gamma_1(\mathbf{x})$ from ADCP horizontal velocities at 130 m depth was used to estimate the location of the anticyclonic eddy center, defined as the location with a minimum value of $\Gamma_1(\mathbf{x})$. Over the month of May, the eddy center translated southward from about 49.1 to 48.7°N (Figure 1). The Lagrangian float, drifting at a parking depth of about 100 m, transcribed a circular motion about this eddy center, with an approximate radius of 5–10 km and a period of about 4 days.

Satellite approaches were also used to calculate the eddy center and compare with the in situ result. The Γ_1 and SLA metrics give predictions of the eddy center as the minimum Γ_1 and maximum SLA, respectively (see Figure 6). The satellite-derived eddy centers were always within 16 km of the in situ eddy center, with an average distance of about 7 km (Figure 1B), which is well within the resolution of the gridded satellite altimetry product. This result is in spite of the reduction in SLA associated with mode water eddies, as interior isopycnals are partially compensated near the surface, making it more difficult to locate this eddy from altimetry. The eddy center from the META3.2 algorithm closely matches the SLA-based eddy center location shown here, since the only difference in the underlying altimetry data is a low-pass spatial filter, and is therefore not independently shown. Using satellite altimetry also enables tracking of the eddy before and after the EXPORTS-NA deployment, showing a slow and steady drift southward of the eddy over time (Figure 1B).

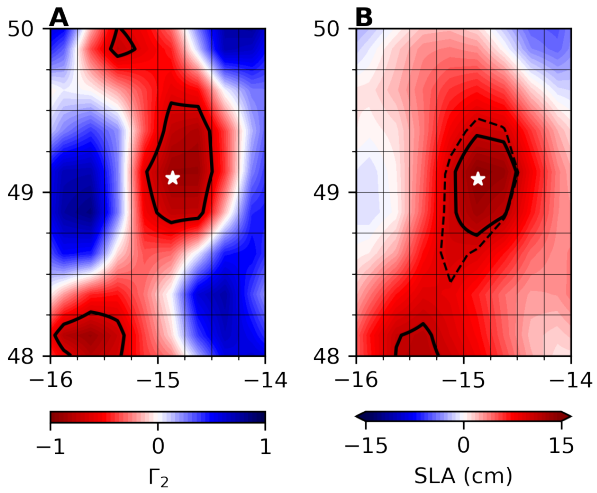

Figure 6. Snapshot of (A) Γ_2 and (B) sea level anomaly (SLA) from 11 May, 2021 calculated from satellite data, with grid lines representing the resolution of the gridded product. In each panel, the black contour represents a proposed threshold (-0.64 for Γ_2 and 11 cm for SLA) and the white star is the eddy center according to each product. In (B), the dashed black line gives the eddy edge from the META3.2 data product (along a given SLA_{filt} contour).

4.2 Eddy spatial extent

The in situ metrics clearly show the eddy as an area around the eddy center with a weakly stratified interior (large h_{iso}) and large amounts of core waters (Figure 7). These eddy-like waters are also confined within a distance from an apparent eddy center, suggesting the use of a simple distance metric. Each of these metrics can be compared to a suitable threshold value to determine if a given profile is within, or outside of, the eddy.

Out of the 664 profiles used here, 456 were within 20 km of the eddy center, and all but two of those had a core isopycnal thickness of over 275 m, designating them as within the eddy. Similarly, all 156 profiles farther than 25 km from the eddy center were designated as outside of the eddy. A threshold value of 22 km minimized the sum of false positive and false negative results and was chosen as the threshold value. This distance threshold correctly classifies 99% (466/471) of the profiles within the eddy, and 97% (168/173) of the profiles outside of the eddy (Figure 8A).

The existence of at least 40 m of core WM in a given profile, defined using potential density and spice thresholds, is another relatively simple metric that correctly identified 98% (461/471) of profiles within the eddy, and 83% (169/173) of profiles outside of the eddy (Figure 8B). This approach therefore has similar skill as compared with the distance metric.

The satellite metrics showed comparable skill at diagnosing when a profile was in an eddy compared with the in situ metrics. The rotational metric Γ_2 indicates the local dominance of anticyclonic rotation, rather than shear, at values less than $-2/\pi \approx -0.64$. This threshold value correctly identifies 100% (471/471) of profiles from within the eddy and 62% (106/171) of profiles outside of the eddy (Figure 8C). The SLA method

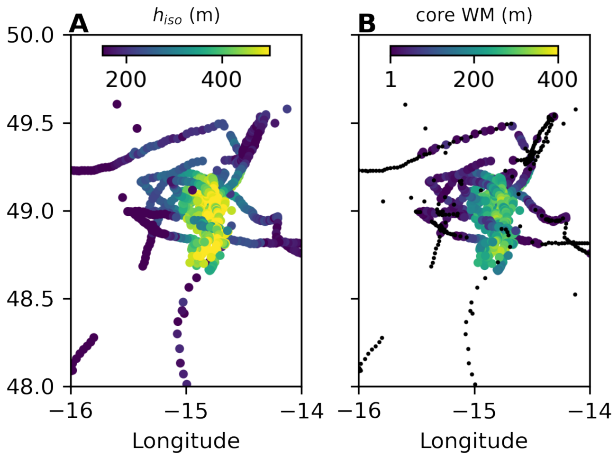

Figure 7. (A) Core isopycnal thickness h_{iso} and (B) width of core WM for each profile (see Table 1). Black dots in panel B indicate waters with no core WM present.

was more accurate than the Γ_2 approach, with 100% (471/471) of profiles within the eddy accurately predicted, as well as 77% (132/171) of profiles outside the eddy (Figure 8E).

In contrast to the in situ metrics defined above, the satellite-based thresholds employing Γ_2 and SLA were not optimized for the highest accuracy. Optimizing Γ_2 and SLA thresholds, as was done for the in situ metrics, would have resulted in only 25 incorrect predictions from Γ_2 (threshold level of -0.75), and 26 from SLA (threshold value from 11.8–12 cm), which represents approximately equivalent skill to the core WM metric and distance metrics.

The META3.2 algorithm is about as accurate as the Γ_2 method, with 100% (471/471) accuracy on profiles within the eddy and 63% (107/171) for those outside the eddy (Figure 8E). This approach uses a time-varying threshold on SLA_{filt} data (see above), ranging from 5.8 to 7.6 cm. The upper limit on this threshold, 7.6 cm, roughly corresponds to the SLA threshold used in Figure 8E of 11 cm, indicating a static, rather than time varying, approach would have resulted in higher accuracy for this eddy.

5 Discussion

This study compares and contrasts methods for determining the location and spatial extent of an anticyclonic eddy in the North Atlantic during May of 2021. Methods using in situ metrics are able to directly capture features of the subsurface ocean where the eddy core is located (Johnson et al., in prep.). Satellite-based products are more coarsely resolved in space, due to the limited number of observations in space and time by nadir-looking satellite altimeters, and can only estimate geostrophic currents. However, they provide a more complete picture of the water surrounding the eddy, rather than only where in situ assets were located, and can track the target eddy for a longer period of time.

5.1 Eddy center from in situ and satellite metrics

Satellite and in situ metrics differed only slightly on where the center of the eddy was located, with the satellite metrics placing the eddy center on average within about 7 km of the in situ observations. Satellite and in situ metrics alike generally remained within the approximate trajectory of the Lagrangian float (Figure 1B), which remained within the eddy throughout the deployment (Johnson et al., in prep.). For the EXPORTS-

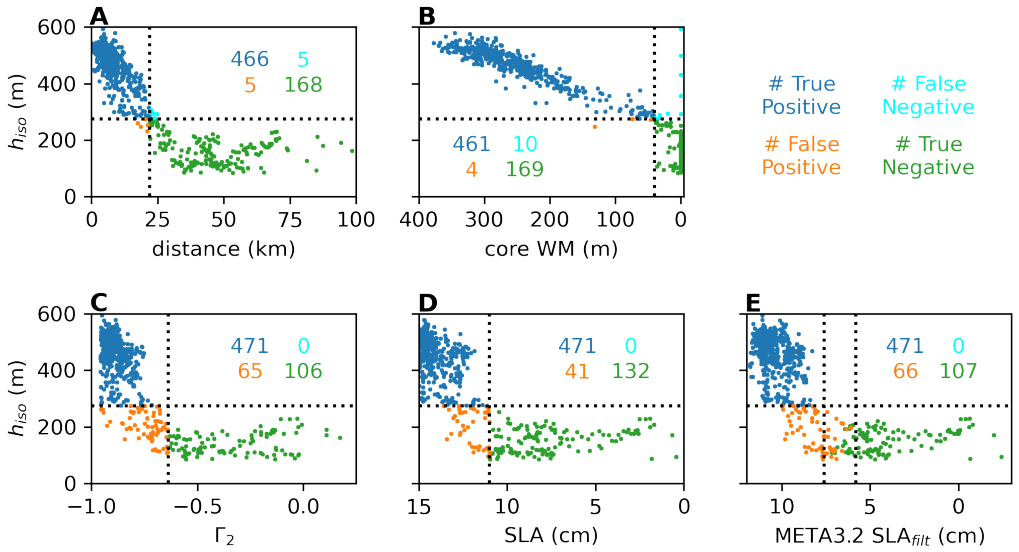

Figure 8. Scatter plot of eddy metrics with respect to the reference of h_{iso} for all profiles (n=644) from 5–30 May that reach at least 27.2 kg m^{-3} and are located between 48–50°N and 14–16°W. Metrics (proposed thresholds as black dotted lines) are: (A) distance from eddy center ($<$ 22 km), (B) vertical extent of core water mass (WM; $>$ 40 m), (C) satellite-based Γ_2 ($<$ $-2/\pi$), (D) satellite-based sea level anomaly (SLA; $>$ 0.115 m), and (E) the META3.2 algorithm, with threshold values of SLA_{filt} from 5.8–7.6 cm. Colors and numbers are associated with true positive (blue), false negative (cyan), false positive (orange), and true negative (green) predictions, where the truth is determined by the threshold metric $h_{iso} > 275$ m.

NA eddy considered here, satellite-based estimates of the eddy center were therefore accurate enough to follow the retentive core of this relatively small eddy. These results also suggest more generally that satellite approaches which locate eddy centers from SLA extremes are adequately able to represent eddy locations to within the retentive centers of the eddies.

5.2 Eddy size from in situ measurements

Six different methods for determining the extent of the eddy were compared, of which three were based on in situ measurements and three were from satellite altimetry. The three in situ metrics agreed with each other well for the available deep profiles: 459 of the 471 (97%) of the profiles within the eddy were identified as such for all in situ metrics, as were 166 of 171 (97%) of profiles outside of the eddy, for a combined accuracy of all in situ metrics of 97%. False eddy predictions for the in situ metrics based on distance and core WM are distributed throughout the region, indicating that there is no significant spatial bias in this prediction (Figure 9A–B).

While the predictions from each of the metrics are similar, they each provide distinct information about the eddy and individually have different advantages. The thickness method, h_{iso}, defined here as the reference method, classifies profiles with low interior stratification as within the eddy. The threshold chosen here, a minimum thickness of 275 m over 0.05 kg m^{-3}, imposes a maximum Brunt-Väisälä frequency within the eddy

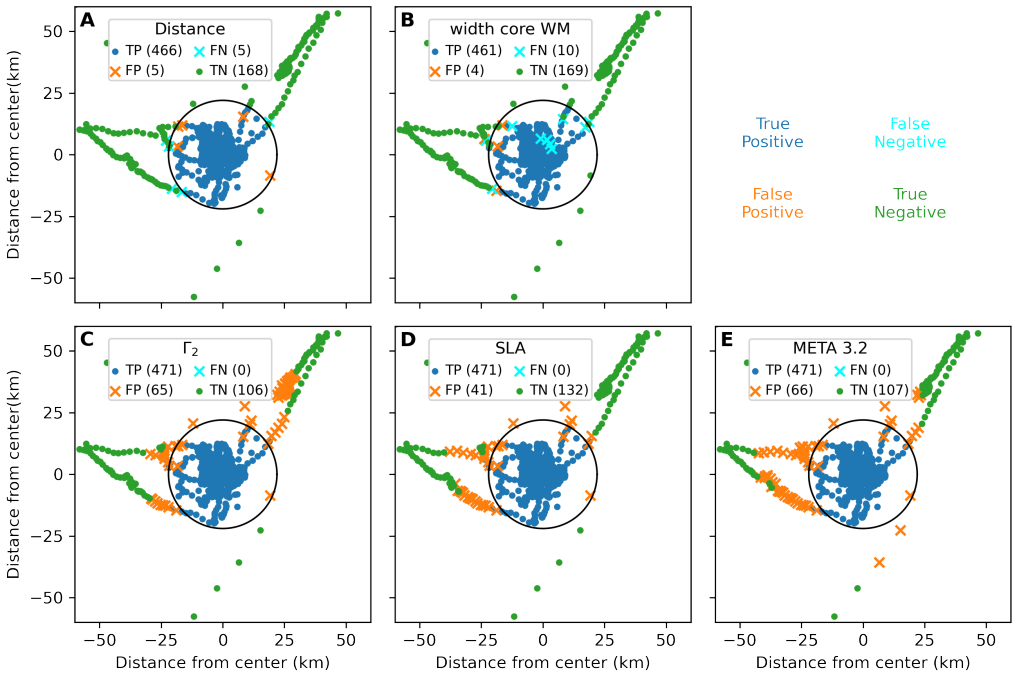

Figure 9. Scatter plot of every "deep" profile (see Table 1) during EXPORTS-NA, colored by the prediction (Positive/Negative) of being within the eddy from (A) distance from eddy center, (B), width of core waters, (C) satellite-derived Γ_2, (D) satellite-derived SLA, and (E) META 3.2, and whether or not that prediction was accurate (True/False) based on a h_{iso} threshold. Black circle in each panel is the 22 km distance threshold.

core of

$$N_2 = b_z = \frac{g}{\rho_0}\frac{\Delta\sigma}{\Delta z} \approx 1.7 \times 10^{-6}\ \mathrm{s}^{-2}, \tag{3}$$

where $g = 9.8$ m s^{-2} is the gravitational acceleration and $\rho_0 = 1027$ kg m^{-3} is a reference density. The maximum Ertel potential vorticity (PV) within the eddy core can be approximated as

$$PV = fN^2 \approx 2 \times 10^{-10}\ \mathrm{s}^{-3}, \tag{4}$$

where $f = 1.1 \times 10^{-4}$ s^{-1} is the planetary vorticity. This definition assumes that the relative vorticity is small compared to f. Assuming an average eddy radius of 22 km and a speed of 20 cm s^{-1} at the eddy edge, the relative vorticity is approximately -0.09×10^{-4} s^{-1}, or less than 10% of the planetary vorticity. This PV threshold aligns well with previous observations of subthermocline eddies in the region (cf. Figure 5 of Thompson et al. (2016)).

Another in situ metric is the existence of core waters, which are defined here by potential density and spice thresholds. Assuming minimal mixing of waters over time, this definition can be used to trace this water mass back in time and find outcropping locations of waters with these characteristics at the surface. This method is also conceptually straightforward, as it directly equates being within an eddy to waters with given physical characteristics.

A critical distinction, however, exists between the spatial extent of the eddy core, considered here, and the spatial extent of the surface waters most identified with this particular eddy. In contrast to the results presented here, Johnson et al. (in prep.) find

a much more diffuse temperature and salinity signal identifying core eddy surface waters, and suggest a smaller radius of 15 km about the eddy center. This difference poses a significant limitation to current eddy tracking efforts: the interior core of the eddy may be distinct from the volume of water trapped by the eddy at the surface, due primarily to wind stress, notably from a series of storms during the deployment (Johnson et al., in prep.). This is especially important for Lagrangian deployments such as EXPORTS-NA that aim to measure biological processes occurring primarily within the euphotic zone.

5.3 Eddy size from satellite observations

The EXPORTS-NA deployment provides an excellent opportunity to evaluate how well satellite altimetry-based algorithms, and especially the widely-distributed META3.2 method (Mason et al., 2014), perform at estimating the extent of one anticyclonic eddy. In general these methods compare well with in situ metrics, despite not being optimized for this particular eddy. False predictions for the satellite metrics are spatially concentrated in a region to the west of the eddy (for Γ_2, SLA, and META 3.2) and to the northeast (for Γ_2; Figure 9C–E). This suggests two possibilities: either the satellite data on the western edge of the eddy is biased due to lack of altimetry data and/or a coarsely-resolved 1/4° data product, or the satellite algorithms accurately depict a western region of the eddy that has similar SLA and is encircled by rotating waters, but nevertheless contains waters with different properties. This second possibility is supported by steric height data calculated from in situ profiles (not shown here), which also suggest a region to the west of the eddy with high SLA. This area to the west of the eddy core has also been shown to have anomalous surface water properties, possibly indicating injection of different waters into the eddy (Johnson et al., in prep.). In contrast, the incorrect predictions on the northeast side of the eddy from the Γ_2 method were due to the apparent merging (only shown in this metric) of this feature with another eddy to the north.

Satellite-based methods for eddy detection and tracking provide the ability to diagnose changes in eddy properties, such as effective radius, circularity or eccentricity, and strength (magnitude of SLA and Γ_1 extremes), over time (Figure 10). The satellite metrics estimate the effective radius of the eddy at 20–40 km at the beginning of the field deployment. The SLA metric shows a gradual increase in the effective radius from 22 km to 37 km over the course of the month of May. This increase is not clearly seen in the other metrics (Γ_2 and META3.2). All, however, agree that the circularity of the eddy, defined as the fraction of area within the eddy that is also within a perfect circle encompassing the same area, decreased from a nearly perfectly circular eddy at the beginning of May to a circularity of 0.7–0.85 by the end of the month. Taken as a whole, these satellite-based results indicate that the eddy sampled during EXPORTS-NA was spreading out and becoming more eccentric throughout May of 2021, consistent with other in situ observations from EXPORTS-NA (Johnson et al., in prep.).

The eddy size from the META3.2 algorithm varied substantially more than that of either of the other satellite methods (Figure 10A). This is a direct result of the way META3.2 determines the threshold SLA_{filt} value, which is to maximize the geostrophic velocity around the eddy edge. This method does not take into account past threshold levels, potentially resulting in large discrepancies from day to day, which will affect size and shape parameters of the eddy. For example, the increase in apparent eddy size from 20–25 May for this algorithm is due to a decrease in the threshold value of SLA_{filt} from 7.25 cm to about 6 cm over this period. These changes in satellite-based SLA_{filt} do not smoothly vary with time and likely will contribute to overestimating variance in eddy parameters using this method.

The central altimetry product used here was a daily SLA field utilizing five satellite altimeters, gridded to 1/4° resolution. Gridded SLA was then interpolated using a

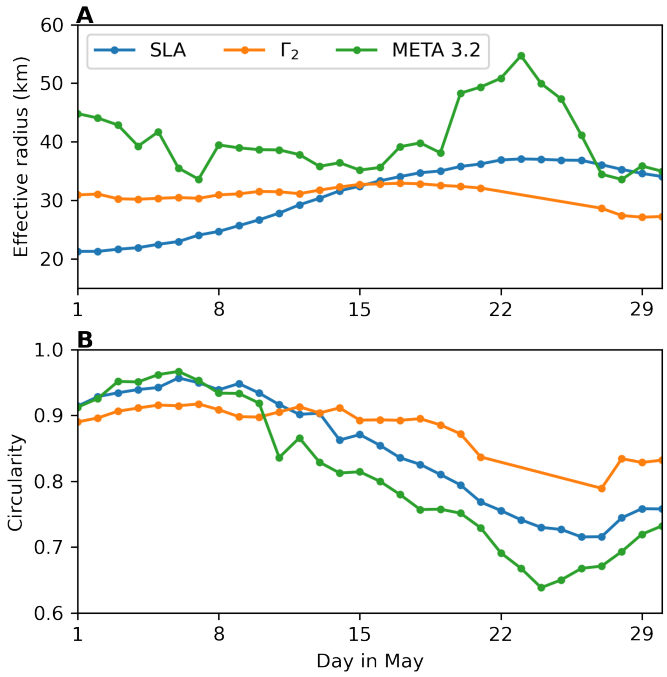

Figure 10. Changes in satellite-based eddy effective radius (A) and circularity (B) for the Γ_2 (orange), SLA (blue), and META 3.2 (green) algorithms. Gaps in the Γ_2 metric indicate when this approach incorrectly merged the study eddy with another nearby eddy, as indicated by a circularity below 0.7 (see text).

cubic spline to the positions of the assets. Which altimetry fields are used, how they are gridded, and how that grid is interpolated are all factors that will influence local SLA values at the positions of the assets. For example, use of a two-altimeter data product, produced to provide a consistent long-term time series of altimetry, severely and detrimentally affected the accuracy of all of the satellite-based predictions. Other gridding procedures have been developed, although not yet implemented for the North Atlantic during EXPORTS-NA. For example, Ubelmann et al. (2015) developed a dynamical mapping algorithm which improves on the standard linear interpolation used here by including nonlinear temporal propagation of sea surface height anomalies. This product has improved skill at accurately estimating sea surface height products (Ballarotta et al., 2020). These newer products are precursors to operational sea surface height data that will be available from the recently-launched Surface Water and Ocean Topography (SWOT) satellite (Morrow et al., 2019).

Machine learning may also lead to improvements in SLA estimation and therefore eddy identification and tracking even from coarser satellite-derived data products. S. Martin et al. (in review) show that incorporating higher-resolution sea surface temperature (SST) measurements into sea surface height gridding algorithms can significantly increase the final accuracy and possible resolution of these final products. For the EXPORTS-NA dataset, the mean SST, here estimated as the average conservative temperature of the upper 20 m from in situ profiles, is significantly different ($p<0.01$) for the false positive regions (12.79 ± 0.31) than for the true positive (12.46 ± 0.16) and true negative (12.60 ± 0.123) regions with respect to the satellite-derived SLA predictions (Figure 9D), suggesting that a product incorporating SST may improve the accuracy of satellite-derived SLA.

5.4 Lessons learned from mapping an eddy

One of the primary challenges in mapping an eddy from in situ measurements is to resolve the depth variability. The core of the EXPORTS-NA eddy was located at about 400 m, and measurements down to at least 800 m were required to fully characterize this feature (Figure 4). Since the EXPORTS-NA deployment was primarily concerned with the biological pump, many of the ship-based profiles did not extend to this depth, and were therefore not used here (Table 1). Part of the challenge is that surface water characteristics were modified during the course of the deployment by several large storms that entered the region (see Johnson et al., in prep.), meaning profiles only near the surface, or underway data from the ships, were less useful in determining the eddy extent.

Transects across the edge of the eddy were also important to distinguish interior water masses from those outside of the eddy, which were used to determine threshold values for isopycnal thickness and the temperature and salinity characteristics that went into characterizing the core WM (e.g., Figure 4). However, in situ characterization of the eddy edge came primarily from three glider transects: two on the western edge and one to the northeast (Figure 9). The lack of knowledge of the eddy boundary to the southeast from in situ measurements limited our ability to fully distinguish between the different satellite metrics. This also highlights the utility of satellite-derived eddy boundaries, which are able to provide estimated values for the entire edge of the eddy (e.g., Figure 6), despite the trade-offs associated with their coarse resolution.

The results here indicate that even for a relatively small eddy, standard satellite-based methods of deriving eddy boundaries, such as META3.2, perform well. However, the EXPORTS-NA eddy was not necessarily a good representative candidate. This eddy was carefully chosen to represent a stable and coherent feature over the course of the field deployment (Erickson et al., 2022), which may have resulted in its being better represented in satellite products than an average eddy. The PAP region is also an area of low variability in sea surface height (Ballarotta et al., 2020) and low error in derived velocities as compared with drifter data (Taburet et al., 2019) compared with, for example, more energetically active western boundary current regions. On the other hand, as a mode water eddy, it had a smaller associated SLA due to interior compensating isopycnal gradients, challenging satellite altimetry algorithms that rely on SLA. A study focused on only one eddy can only provide suggestive evidence on the utility of altimetry methods for determining eddy boundaries, and a more comprehensive survey of eddy edges from in situ and satellite measurements is needed.

6 Conclusions

The EXPORTS-NA field program was conducted within and around an anticyclonic mode water eddy. Profiles of temperature and salinity from ships, gliders, and BGC floats deployed as part of this project allow different methods of detecting eddies from in situ and satellite methods to be tested. A key characteristic of an anticyclonic mode water eddy is shoaling lighter isopycnals and deepening denser isopycnals, motivating the use of the thickness of the 27.15–27.2 kg m^{-3} layer as a metric for the eddy, along with a water mass characteristic determined by the temperature and salinity, or equivalently the potential density and spice, of measured waters. Each of these metrics did well at accurately predicting the eddy. Velocity-based metrics from in situ measurements and from satellite-based altimetry give similar results, suggesting that even comparably low satellite resolution can accurately track even relatively small eddies, with radii on the scale of the gridded data product itself.

For this eddy, the data collected here support the use of algorithms based on satellite algorithms in future eddy tracking studies. Satellite altimetry is able to provide information on changes in eddy properties over time and space that are not possible even

with hundreds of in situ profiles taken as a result of the EXPORTS-NA deployment. However, there are challenges to these altimetry-based methods. At least for this eddy, these challenges related less to the coarse resolution of altimetry maps, and were more related to the ability of sea level contours to reliably demarcate eddy boundaries. In addition, a commonly-used algorithm, META3.2, re-calculates the SLA contour associated with the eddy edge each day, leading to significant jumps in eddy size that are likely unphysical. Here we therefore suggest a constant, or perhaps smoothly time-varying, SLA contour approach that was shown to more accurately represent the edge of the eddy, as compared with in situ measurements. This SLA contour can be found using a method that calculates the average rotation about each point in space, and calculates the eddy center as the point associated with the maximum level of rotation. This approach is generalizable to any other eddy using satellite altimetry measurements, and in future work will be applied to a variety of other datasets sampling eddies throughout the ocean.

Data Availability

The in situ data collected by the EXPORTS-NA project can be found in the SeaBASS repository at `https://seabass.gsfc.nasa.gov/cruise/EXPORTSNA`. Satellite altimetry was provided by the Copernicus Marine Environmental Monitoring Service (CMEMS), and the META3.2 analysis was provided by AVISO (Archiving, Validation and Interpretation of Satellite Oceanographic data). Code to process ADCP measurements was provided by Common Ocean Data Access System (CODAS) processing code built, run, and maintained by the University of Hawaii Data Acquisition System (UHDAS) and available at `https://currents.soest.hawaii.edu/uhdas_home/`.

Acknowledgments

The authors would like to gratefully acknowledge the efforts of the captains and crews of the *RRS Discovery*, *RRS James Cook*, and *R/V Sarmiento de Gamboa*, as well as those of the entire EXPORTS science team. This field deployment was funded by the NASA Ocean Biology and Biogeochemistry program and the National Science Foundation Biological and Chemical Oceanography programs. Initial gliders deployments were performed by the RRS Discovery and the authors thank the Porcupine Abyssal Plain – Sustained Observatory of the Natural Environment Research Council (NERC, UK), which is principally funded through the Climate Linked Atlantic Sector Science (CLASS) project supported by NERC National Capability funding (NE/R015953/1) and by IFADO (Innovation in the Framework of the Atlantic Deep Ocean) EAPA_165/2016. Technical assistance with the Slocum glider deployment and quality control was provided by Filipa Carvalho (NOC) and Marine Autonomous Robotic Systems (NOC). Assistance and quality control of the Seagliders was provided by Geoff Shilling (UW) and Craig Lee (UW). Z.K. Erickson would like to thank Scott Martin (UW) for valuable conversations about satellite altimetry products. This is PMEL Contribution Number 5444.

References

Abernathey, R., & Haller, G. (2018). Transport by Lagrangian vortices in the Eastern Pacific. *Journal of Physical Oceanography*, *48*(3), 667–685.

Alkire, M. B., D'Asaro, E., Lee, C., Perry, M. J., Gray, A., Cetinić, I., ... others (2012). Estimates of net community production and export using high-resolution, Lagrangian measurements of O_2, NO_3^-, and POC through the evolution of a spring diatom bloom in the North Atlantic. *Deep Sea Research Part I: Oceanographic Research Papers*, *64*, 157–174.

Archer, M., Schaeffer, A., Keating, S., Roughan, M., Holmes, R., & Siegelman, L. (2020). Observations of submesoscale variability and frontal subduction within the mesoscale eddy field of the Tasman Sea. *Journal of Physical Oceanography*,

50(5), 1509–1529.

Ballarotta, M., Ubelmann, C., Pujol, M.-I., Taburet, G., Fournier, F., Legeais, J.-F., ... Picot, N. (2019). On the resolutions of ocean altimetry maps. *Ocean Science*, *15*(4), 1091–1109.

Ballarotta, M., Ubelmann, C., Rogé, M., Fournier, F., Faugère, Y., Dibarboure, G., ... Picot, N. (2020). Dynamic mapping of along-track ocean altimetry: Performance from real observations. *Journal of Atmospheric and Oceanic Technology*, *37*(9), 1593–1601.

Bol, R., Henson, S. A., Rumyantseva, A., & Briggs, N. (2018). High-frequency variability of small-particle carbon export flux in the Northeast Atlantic. *Global Biogeochemical Cycles*, *32*(12), 1803–1814.

Brannigan, L. (2016). Intense submesoscale upwelling in anticyclonic eddies. *Geophysical Research Letters*, *43*(7), 3360–3369.

Brannigan, L., Marshall, D. P., Garabato, A. C. N., Nurser, A. G., & Kaiser, J. (2017). Submesoscale instabilities in mesoscale eddies. *Journal of Physical Oceanography*, *47*(12), 3061–3085.

Chaigneau, A., & Pizarro, O. (2005). Eddy characteristics in the eastern South Pacific. *Journal of Geophysical Research: Oceans*, *110*(C6).

Chelton, D. B., Schlax, M. G., & Samelson, R. M. (2011). Global observations of nonlinear mesoscale eddies. *Progress in Oceanography*, *91*(2), 167–216.

Chelton, D. B., Schlax, M. G., Samelson, R. M., & de Szoeke, R. A. (2007). Global observations of large oceanic eddies. *Geophysical Research Letters*, *34*(15).

Claustre, H., Johnson, K. S., & Takeshita, Y. (2020). Observing the global ocean with Biogeochemical-Argo. *Annual Review of Marine Science*, 23–48.

Damerell, G. M., Heywood, K. J., Thompson, A. F., Binetti, U., & Kaiser, J. (2016). The vertical structure of upper ocean variability at the Porcupine Abyssal Plain during 2012–2013. *Journal of Geophysical Research: Oceans*, *121*(5), 3075–3089.

D'Asaro, E. A. (2003). Performance of autonomous Lagrangian floats. *Journal of Atmospheric and Oceanic Technology*, *20*(6), 896–911.

Della Penna, A., & Gaube, P. (2019). Overview of (sub) mesoscale ocean dynamics for the NAAMES field program. *Frontiers in Marine Science*, *6*, 384.

Dickey, T., Marra, J., Granata, T., Langdon, C., Hamilton, M., Wiggert, J., ... Bratkovich, A. (1991). Concurrent high resolution bio-optical and physical time series observations in the sargasso sea during the spring of 1987. *Journal of Geophysical Research: Oceans*, *96*(C5), 8643–8663.

d'Ovidio, F., De Monte, S., Della Penna, A., Cotté, C., & Guinet, C. (2013). Ecological implications of eddy retention in the open ocean: A Lagrangian approach. *Journal of Physics A: Mathematical and Theoretical*, *46*(25), 254023.

Ellwood, M. J., Strzepek, R. F., Strutton, P. G., Trull, T. W., Fourquez, M., & Boyd, P. W. (2020). Distinct iron cycling in a Southern Ocean eddy. *Nature Communications*, *11*(1), 1–8.

Erickson, Z. K., Fields, E., Omand, M. M., Johnson, L., Thompson, A. F., D'Asaro, E. A., ... Siegel, D. A. (2022). EXPORTS North Atlantic eddy tracking. *NASA Technical Memorandum*, 1–40. doi: 10.1575/1912/29464

Erickson, Z. K., & Thompson, A. F. (2018). The seasonality of physically driven export at submesoscales in the northeast Atlantic Ocean. *Global Biogeochemical Cycles*, *32*(8), 1144–1162.

Erickson, Z. K., Thompson, A. F., Callies, J., Yu, X., Garabato, A. N., & Klein, P. (2020). The vertical structure of open-ocean submesoscale variability during a full seasonal cycle. *Journal of Physical Oceanography*, *50*(1), 145–160.

Estapa, M., Feen, M., & Breves, E. (2019). Direct observations of biological carbon export from profiling floats in the subtropical North Atlantic. *Global Biogeochemical Cycles*, *33*(3), 282–300.

Faghmous, J. H., Frenger, I., Yao, Y., Warmka, R., Lindell, A., & Kumar, V. (2015).

A daily global mesoscale ocean eddy dataset from satellite altimetry. *Scientific data*, *2*(1), 1–16.

Falkowski, P. G., Ziemann, D., Kolber, Z., & Bienfang, P. K. (1991). Role of eddy pumping in enhancing primary production in the ocean. *Nature*, *352*(6330), 55–58.

Firing, E., & Hummon, J. (2010). *Shipboard ADCP measurements.* Retrieved from `https://repository.oceanbestpractices.org/handle/11329/385`

Freilich, M. A., & Mahadevan, A. (2019). Decomposition of vertical velocity for nutrient transport in the upper ocean. *Journal of Physical Oceanography*, *49*(6), 1561–1575.

Frigstad, H., Henson, S., Hartman, S., Omar, A., Jeansson, E., Cole, H., ... Lampitt, R. (2015). Links between surface productivity and deep ocean particle flux at the Porcupine Abyssal Plain sustained observatory. *Biogeosciences*, *12*(19), 5885–5897.

Goni, G. J., & Johns, W. E. (2001). A census of North Brazil current rings observed from TOPEX/POSEIDON altimetry: 1992–1998. *Geophysical Research Letters*, *28*(1), 1–4.

Graftieaux, L., Michard, M., & Grosjean, N. (2001). Combining PIV, POD and vortex identification algorithms for the study of unsteady turbulent swirling flows. *Measurement Science and Technology*, *12*(9), 1422.

Haller, G., Hadjighasem, A., Farazmand, M., & Huhn, F. (2016). Defining coherent vortices objectively from the vorticity. *Journal of Fluid Mechanics*, *795*, 136–173.

Hartman, S. E., Lampitt, R. S., Larkin, K. E., Pagnani, M., Campbell, J., Gkritzalis, T., ... Lankester, S. (2012). The Porcupine Abyssal Plain fixed-point sustained observatory (PAP-SO): Variations and trends from the Northeast Atlantic fixed-point time-series. *ICES Journal of Marine Science*, *69*(5), 776–783.

Heywood, R., & Priddle, J. (1987). Retention of phytoplankton by an eddy. *Continental Shelf Research*, *7*(8), 937–955.

Isern-Fontanet, J., Font, J., García-Ladona, E., Emelianov, M., Millot, C., & Taupier-Letage, I. (2004). Spatial structure of anticyclonic eddies in the Algerian basin (Mediterranean Sea) analyzed using the Okubo-Weiss parameter. *Deep Sea Research Part II: Topical Studies in Oceanography*, *51*(25-26), 3009–3028.

Isern-Fontanet, J., García-Ladona, E., & Font, J. (2003). Identification of marine eddies from altimetric maps. *Journal of Atmospheric and Oceanic Technology*, *20*(5), 772–778.

Jing, Z., Fox-Kemper, B., Cao, H., Zheng, R., & Du, Y. (2021). Submesoscale fronts and their dynamical processes associated with symmetric instability in the Northwest Pacific subtropical ocean. *Journal of Physical Oceanography*, *51*(1), 83–100.

Johnson, L., Siegel, D. A., Carvalho, F., Cetinic, I., Erickson, Z., D'Asaro, E., ... Thompson, A. (in prep.). Overview of the NASA EXPORTS North Atlantic field campaign. *Elementa: Science of the Anthropocene*.

Martin, A., & Pondaven, P. (2003). On estimates for the vertical nitrate flux due to eddy pumping. *Journal of Geophysical Research: Oceans*, *108*(C11).

Martin, S., Manucharyan, G., & Klein, P. (in review). Asynthesizing sea surface temperature and satellite altimetry observations using deep learning improves the accuracy and resolution of gridded sea surface height anomalies..

Mason, E., Pascual, A., & McWilliams, J. C. (2014). A new sea surface height-based code for oceanic mesoscale eddy tracking. *Journal of Atmospheric and Oceanic Technology*, *31*(5), 1181–1188.

McDougall, T. J., & Krzysik, O. A. (2015). Spiciness. *Journal of Marine Research*, *73*(5), 141–152.

McGillicuddy Jr, D. J. (2015). Formation of intrathermocline lenses by eddy-wind interaction. *Journal of Physical Oceanography*, *45*(2), 606–612.

Morrow, R., Fu, L.-L., Ardhuin, F., Benkiran, M., Chapron, B., Cosme, E., ... Zaron, E. D. (2019). Global observations of fine-scale ocean surface topography with the Surface Water and Ocean Topography (SWOT) mission. *Frontiers in Marine Science*, *6*, 232.

Pegliasco, C., Delepoulle, A., Mason, E., Morrow, R., Faugère, Y., & Dibarboure, G. (2022). META3.1exp: A new global mesoscale eddy trajectory atlas derived from altimetry. *Earth System Science Data*, *14*(3), 1087–1107.

Pujol, M.-I., Faugère, Y., Taburet, G., Dupuy, S., Pelloquin, C., Ablain, M., & Picot, N. (2016). DUACS DT2014: The new multi-mission altimeter data set reprocessed over 20 years. *Ocean Science*, *12*(5), 1067–1090.

Richardson, P. (1993). A census of eddies observed in North Atlantic SOFAR float data. *Progress in Oceanography*, *31*(1), 1–50.

Siegel, D. A., Buesseler, K. O., Behrenfeld, M. J., Benitez-Nelson, C. R., Boss, E., Brzezinski, M. A., ... Steinberg, D. K. (2016). Prediction of the export and fate of global ocean net primary production: The EXPORTS science plan. *Frontiers in Marine Science*, *3*, 22.

Siegel, D. A., McGillicuddy Jr, D. J., & Fields, E. A. (1999). Mesoscale eddies, satellite altimetry, and new production in the Sargasso Sea. *Journal of Geophysical Research: Oceans*, *104*(C6), 13359–13379.

Taburet, G., Sanchez-Roman, A., Ballarotta, M., Pujol, M.-I., Legeais, J.-F., Fournier, F., ... Dibarboure, G. (2019). DUACS DT2018: 25 years of reprocessed sea level altimetry products. *Ocean Science*, *15*(5), 1207–1224.

Thompson, A. F. (2022). *EXPORTS calibration document.*

Thompson, A. F., Lazar, A., Buckingham, C., Garabato, A. C. N., Damerell, G. M., & Heywood, K. J. (2016). Open-ocean submesoscale motions: A full seasonal cycle of mixed layer instabilities from gliders. *Journal of Physical Oceanography*, *46*(4), 1285–1307.

Ubelmann, C., Klein, P., & Fu, L.-L. (2015). Dynamic interpolation of sea surface height and potential applications for future high-resolution altimetry mapping. *Journal of Atmospheric and Oceanic Technology*, *32*(1), 177–184.

Whitt, D. B., Lévy, M., & Taylor, J. R. (2019). Submesoscales enhance storm-driven vertical mixing of nutrients: Insights from a biogeochemical large eddy simulation. *Journal of Geophysical Research: Oceans*, *124*(11), 8140–8165.

Wright, D., Pawlowicz, R., McDougall, T., Feistel, R., & Marion, G. (2011). Absolute Salinity, "Density Salinity" and the Reference-Composition Salinity Scale: present and future use in the seawater standard TEOS-10. *Ocean Science*, *7*(1), 1–26.

Figure 1.

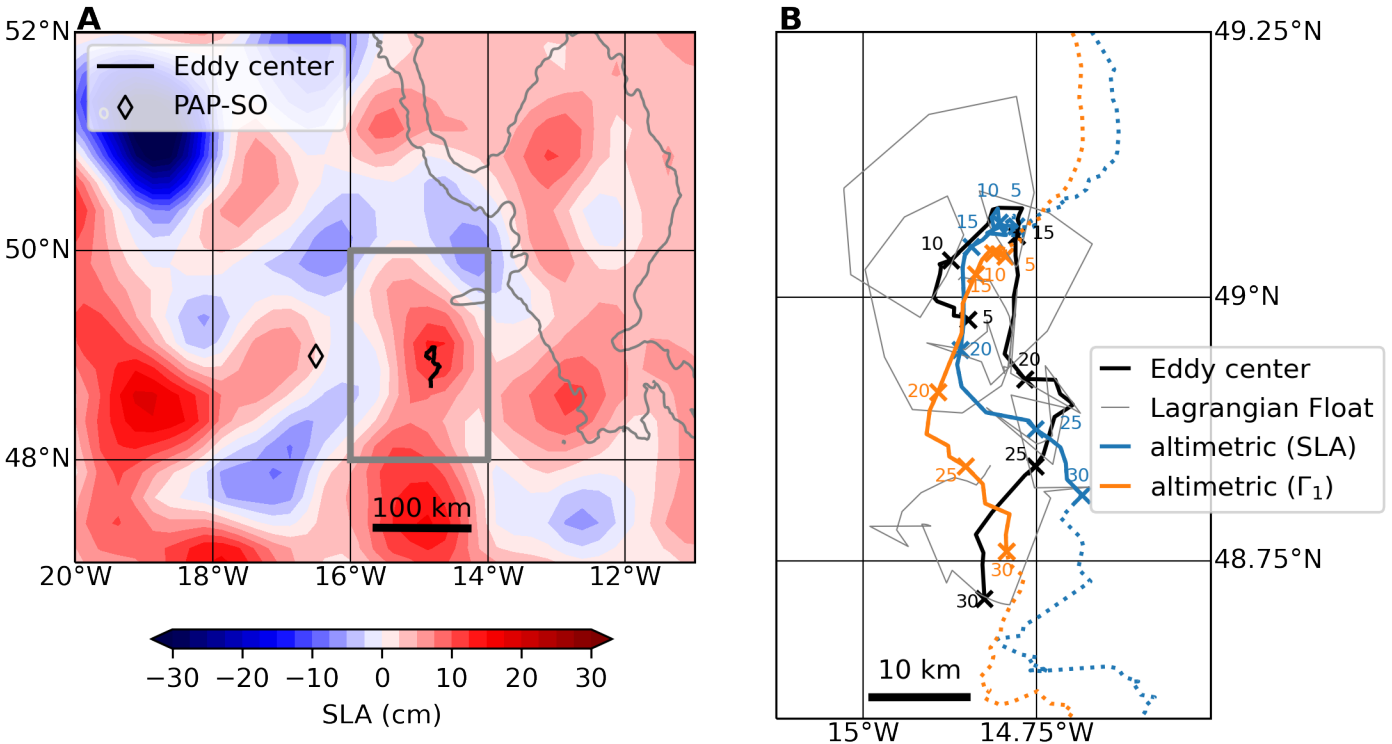
A
52°N
50°N
48°N
20°W
18°W
16°W
14°W
12°W
Eddy center
PAP-SO
100 km
−30 −20 −10 0 10 20 30
SLA (cm)
B
49.25°N
49°N
48.75°N
15°W
14.75°W
Eddy center
Lagrangian Float
altimetric (SLA)
altimetric (Γ1)
10 km

Figure 2.

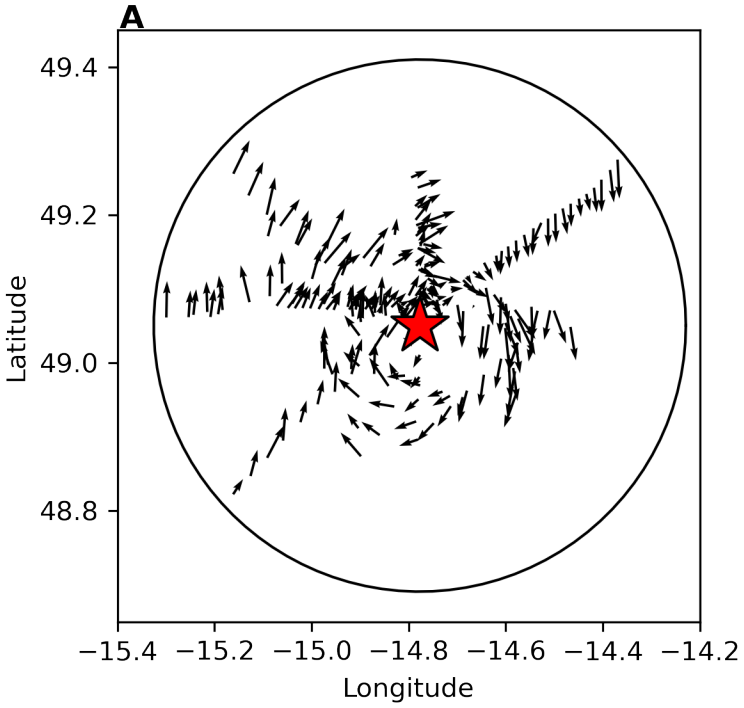
A
49.4
49.2
49.0
48.8
Latitude
−15.4
−15.2
−15.0
−14.8
−14.6
−14.4
−14.2
Longitude

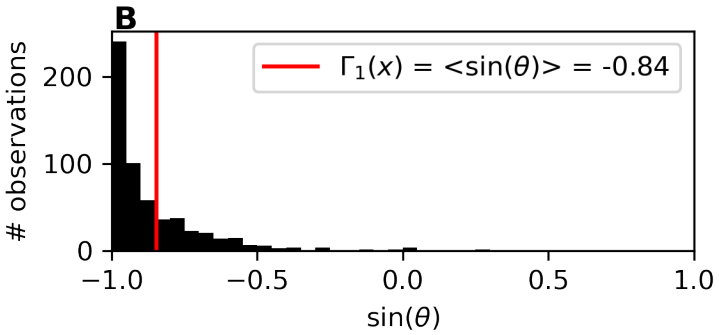
B
Γ1(x) = <sin(θ)> = -0.84
observations
200
100
0
−1.0
−0.5
0.0
0.5
1.0
sin(θ)

Figure 3.

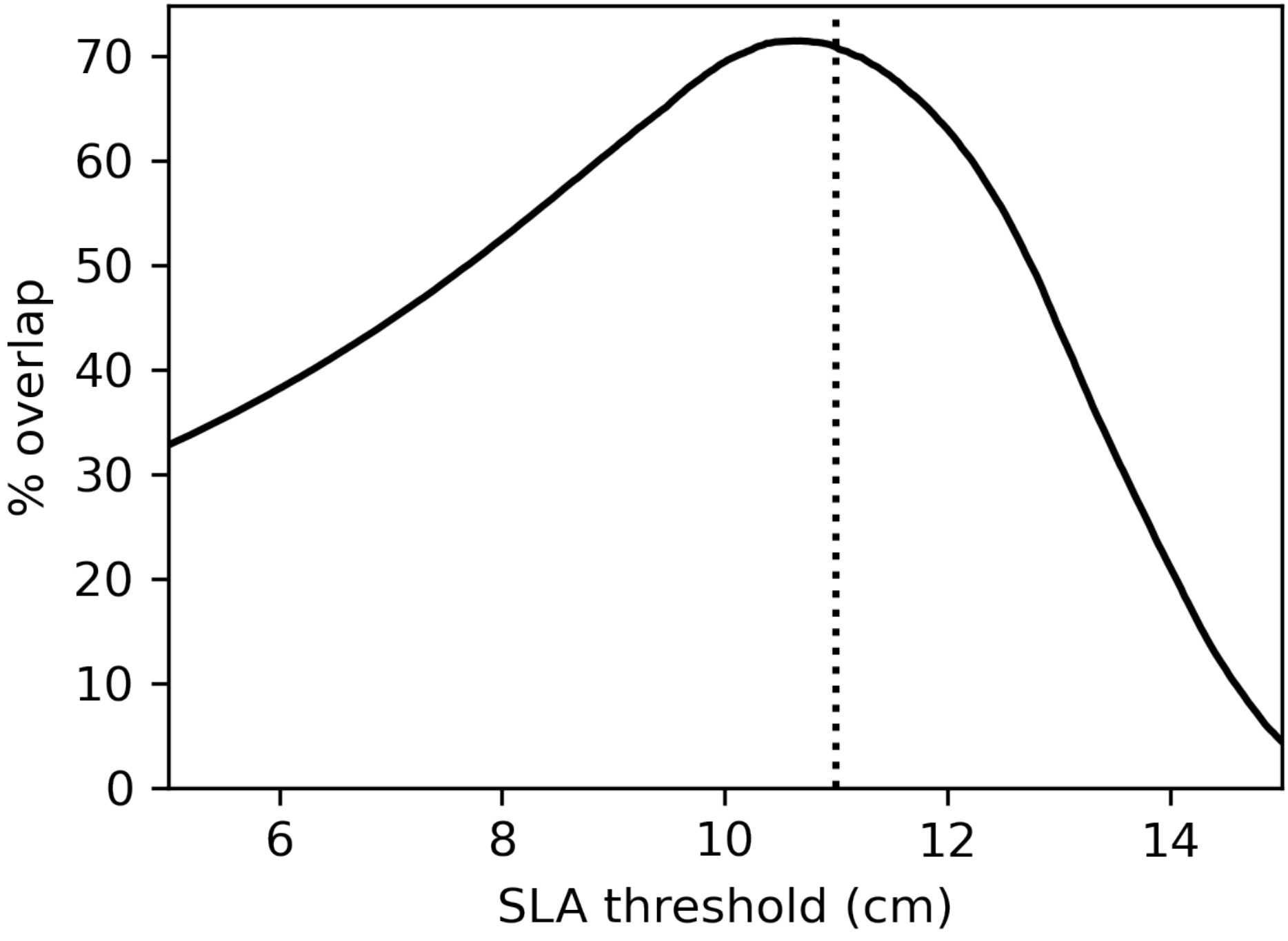
70
60
50
40
30
20
10
0
% overlap
6
8
10
12
14
SLA threshold (cm)

Figure 4.

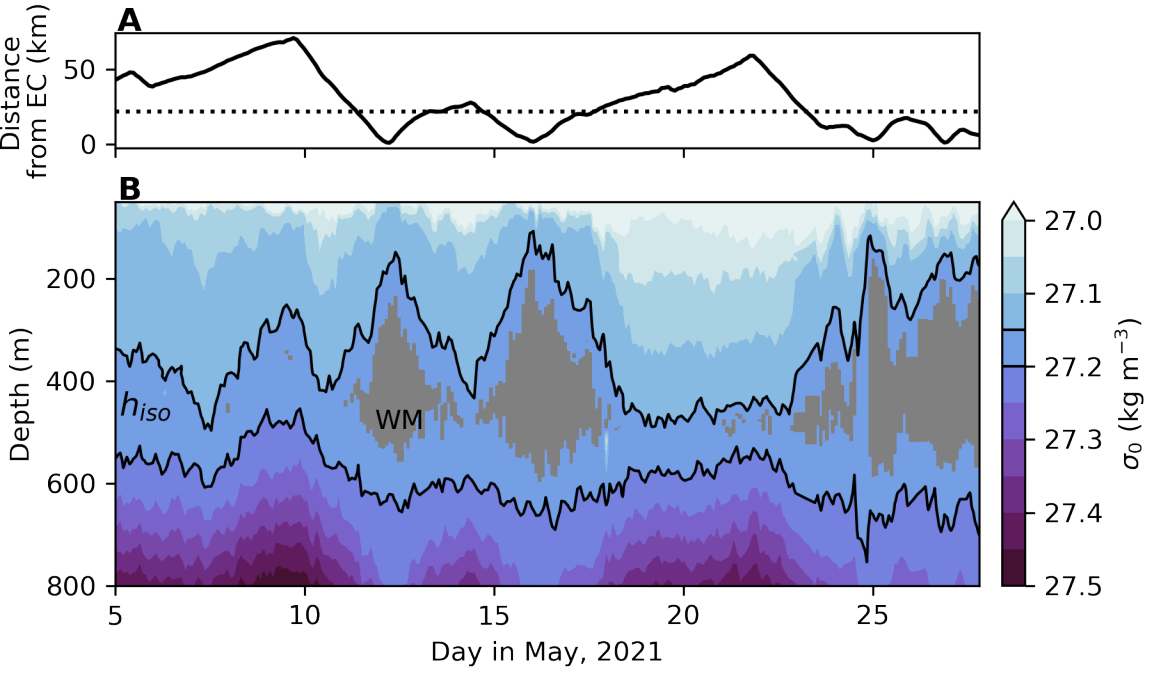
A
Distance from EC (km)
50
0
B
Depth (m)
200
400
600
800
h_{iso}
WM
5
10
15
20
25
Day in May, 2021
27.0
27.1
27.2
27.3
27.4
27.5
σ_0 (kg m^{-3})

Figure 5.

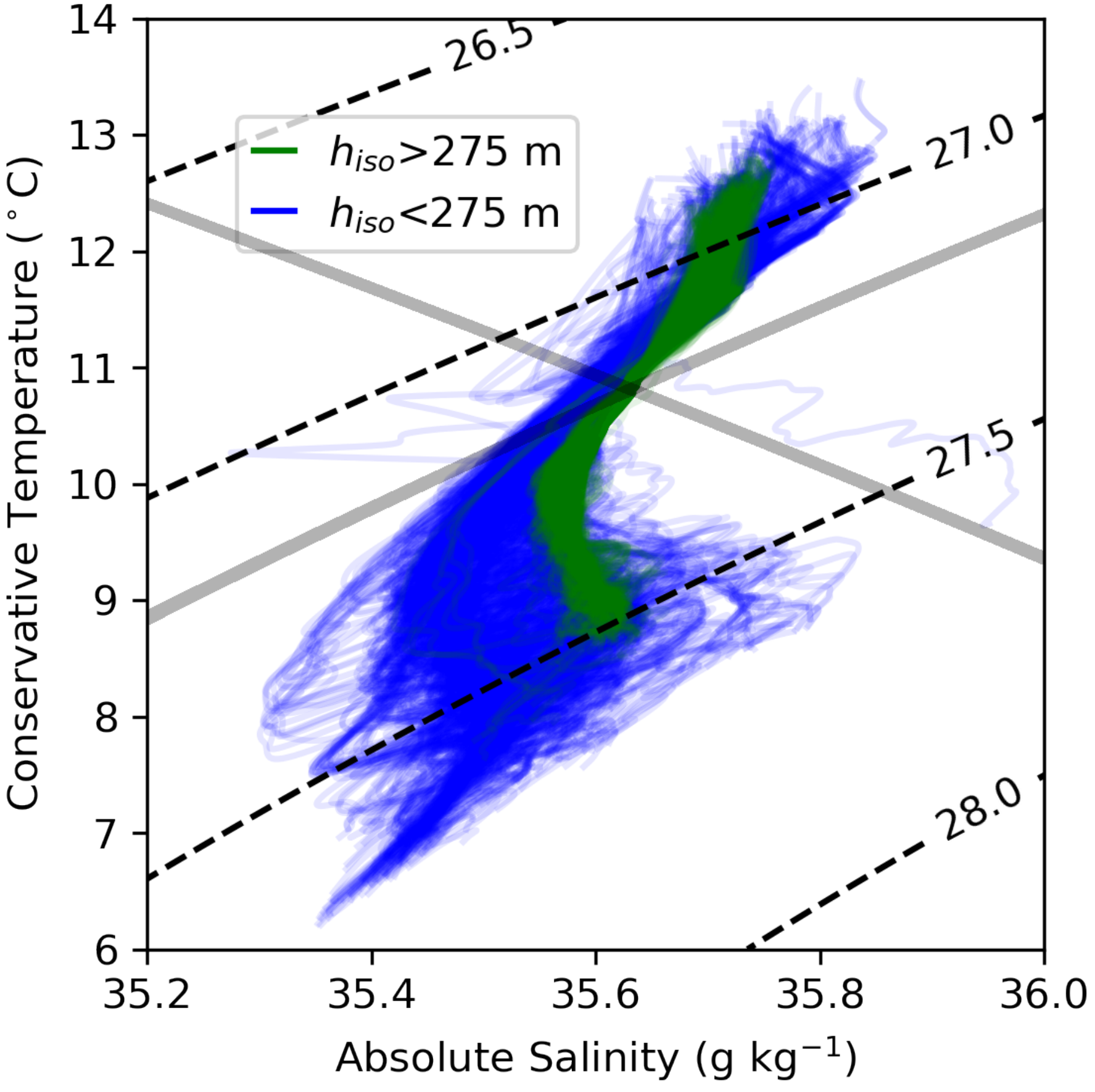
14
13
12
11
10
9
8
7
6
Conservative Temperature (°C)
35.2
35.4
35.6
35.8
36.0
Absolute Salinity (g kg^{-1})
h_{iso}>275 m
h_{iso}<275 m
26.5
27.0
27.5
28.0

Figure 6.

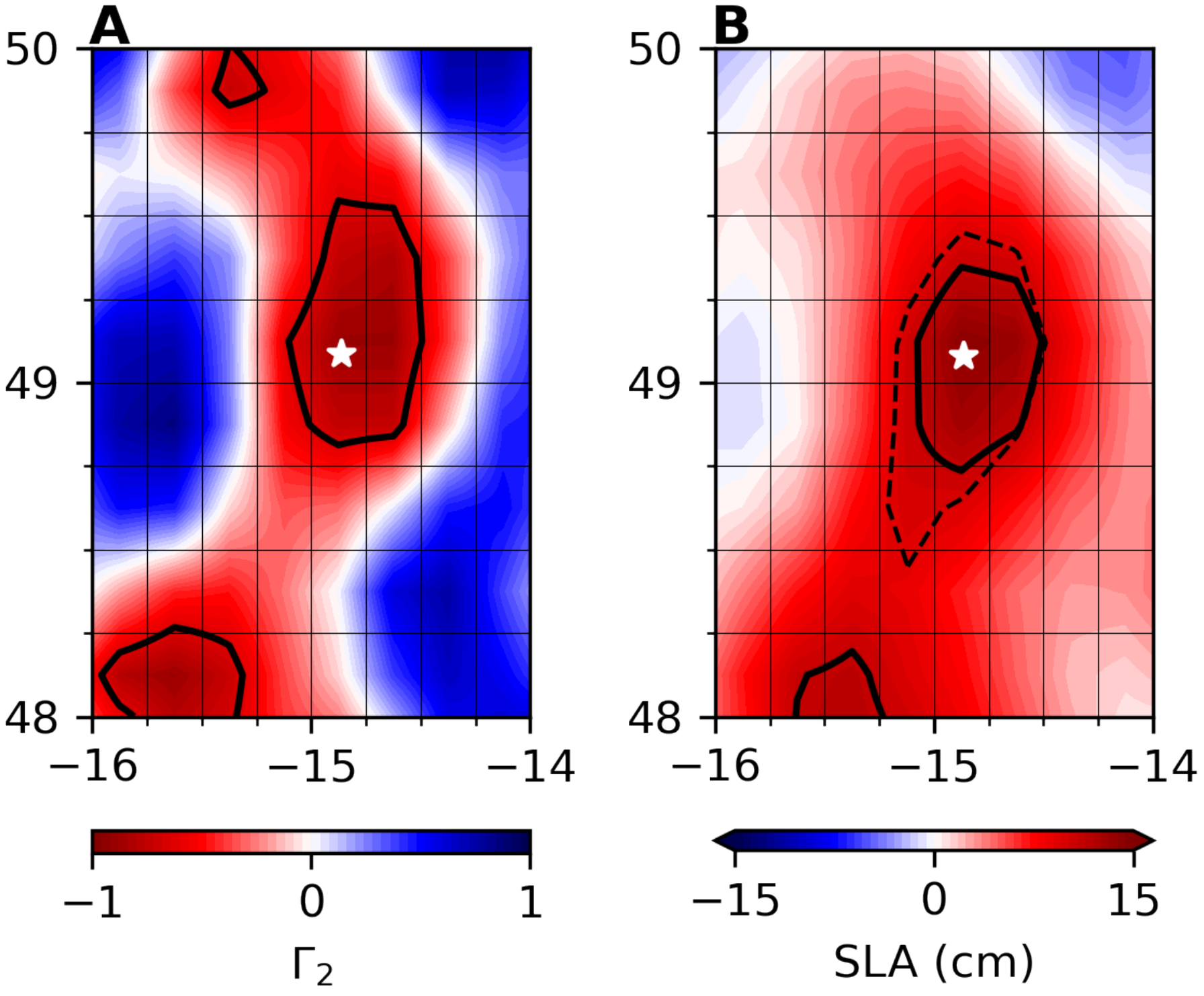
A
B
50
49
48
−16
−15
−14
−1
0
1
Γ_2
−15
0
15
SLA (cm)

Figure 7.

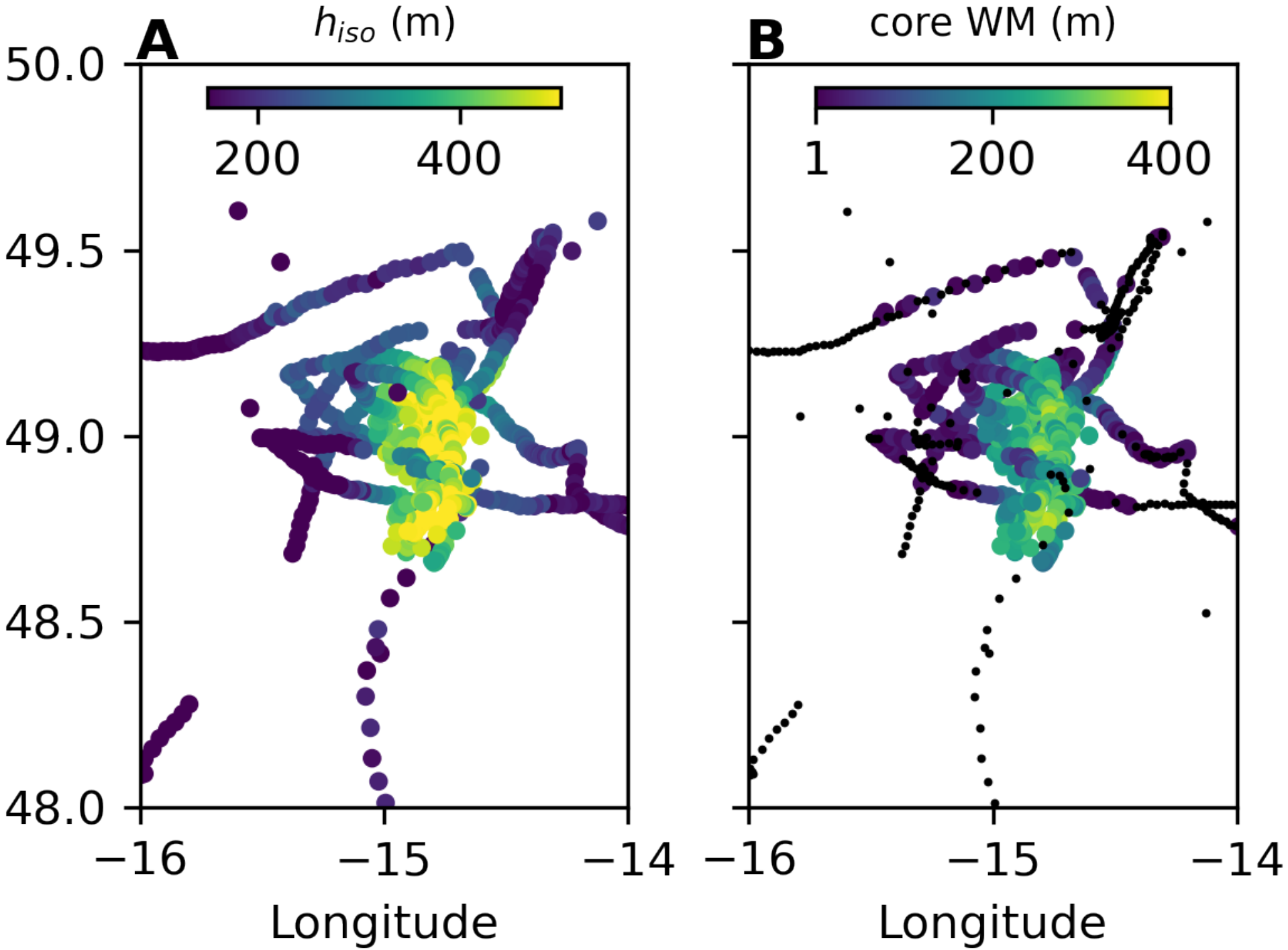
A
h_{iso} (m)
200
400
50.0
49.5
49.0
48.5
48.0
−16
−15
−14
Longitude
B
core WM (m)
1
200
400
−16
−15
−14
Longitude

Figure 8.

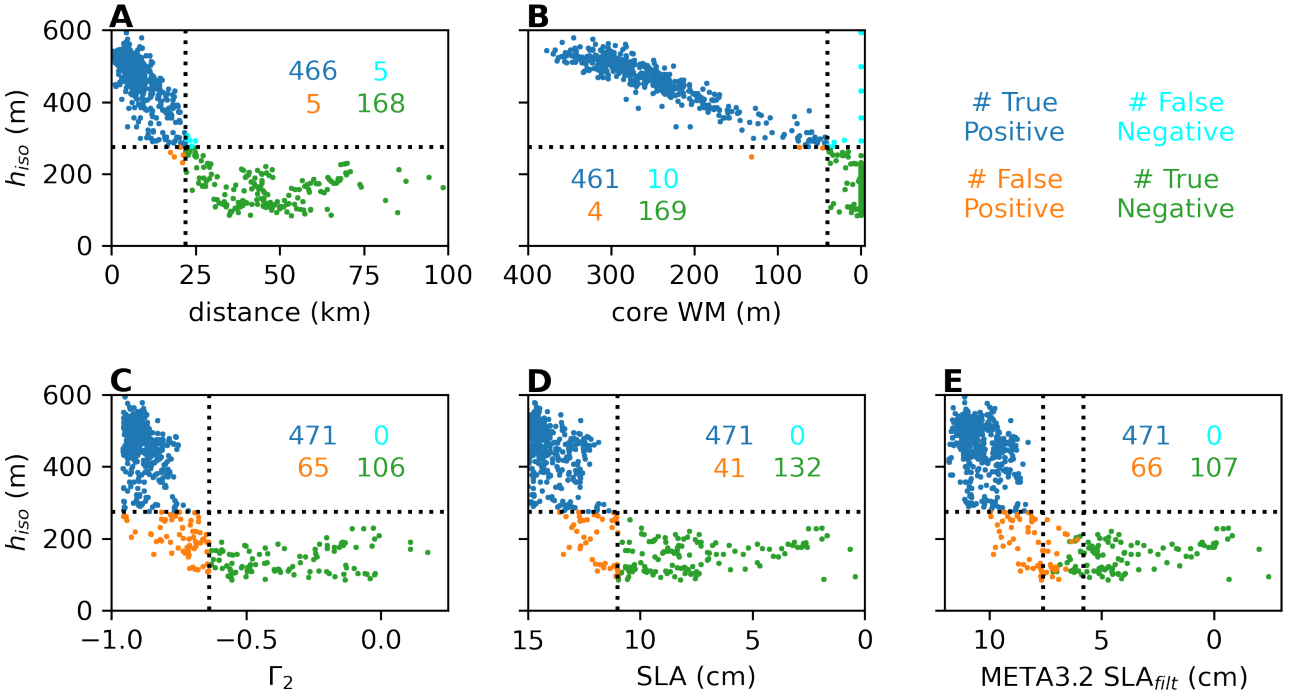
A
B
C
D
E
600
400
200
0
h_{iso} (m)
466 5
5 168
0 25 50 75 100
distance (km)
461 10
4 169
400 300 200 100 0
core WM (m)
True Positive
False Negative
False Positive
True Negative
471 0
65 106
−1.0 −0.5 0.0
Γ_2
471 0
41 132
15 10 5 0
SLA (cm)
471 0
66 107
10 5 0
META3.2 SLA_{filt} (cm)

Figure 9.

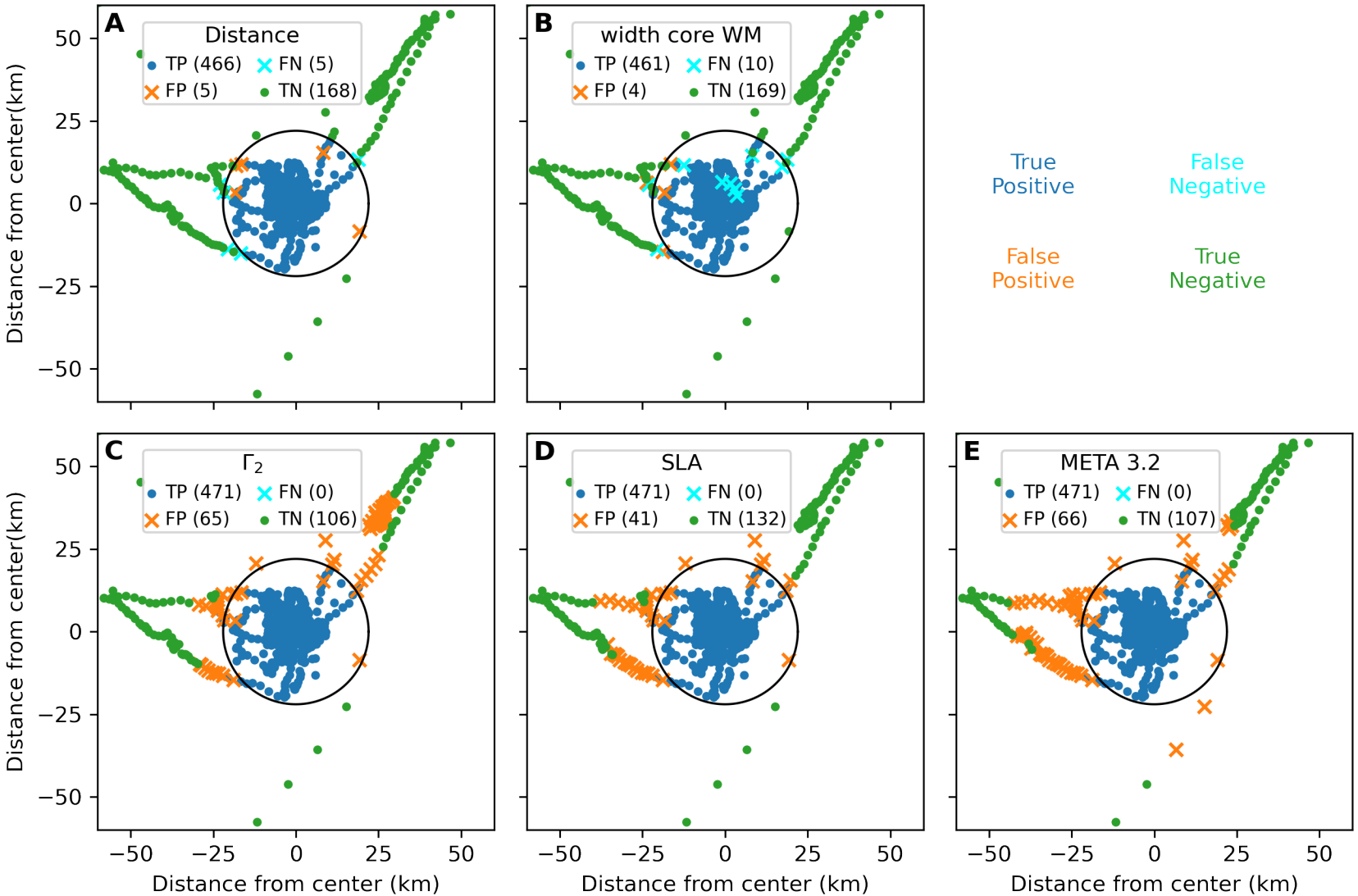
A
Distance
TP (466)
FN (5)
FP (5)
TN (168)
B
width core WM
TP (461)
FN (10)
FP (4)
TN (169)
True Positive
False Negative
False Positive
True Negative
C
Γ_2
TP (471)
FN (0)
FP (65)
TN (106)
D
SLA
TP (471)
FN (0)
FP (41)
TN (132)
E
META 3.2
TP (471)
FN (0)
FP (66)
TN (107)
Distance from center(km)
Distance from center (km)
50
25
0
−25
−50

Figure 10.

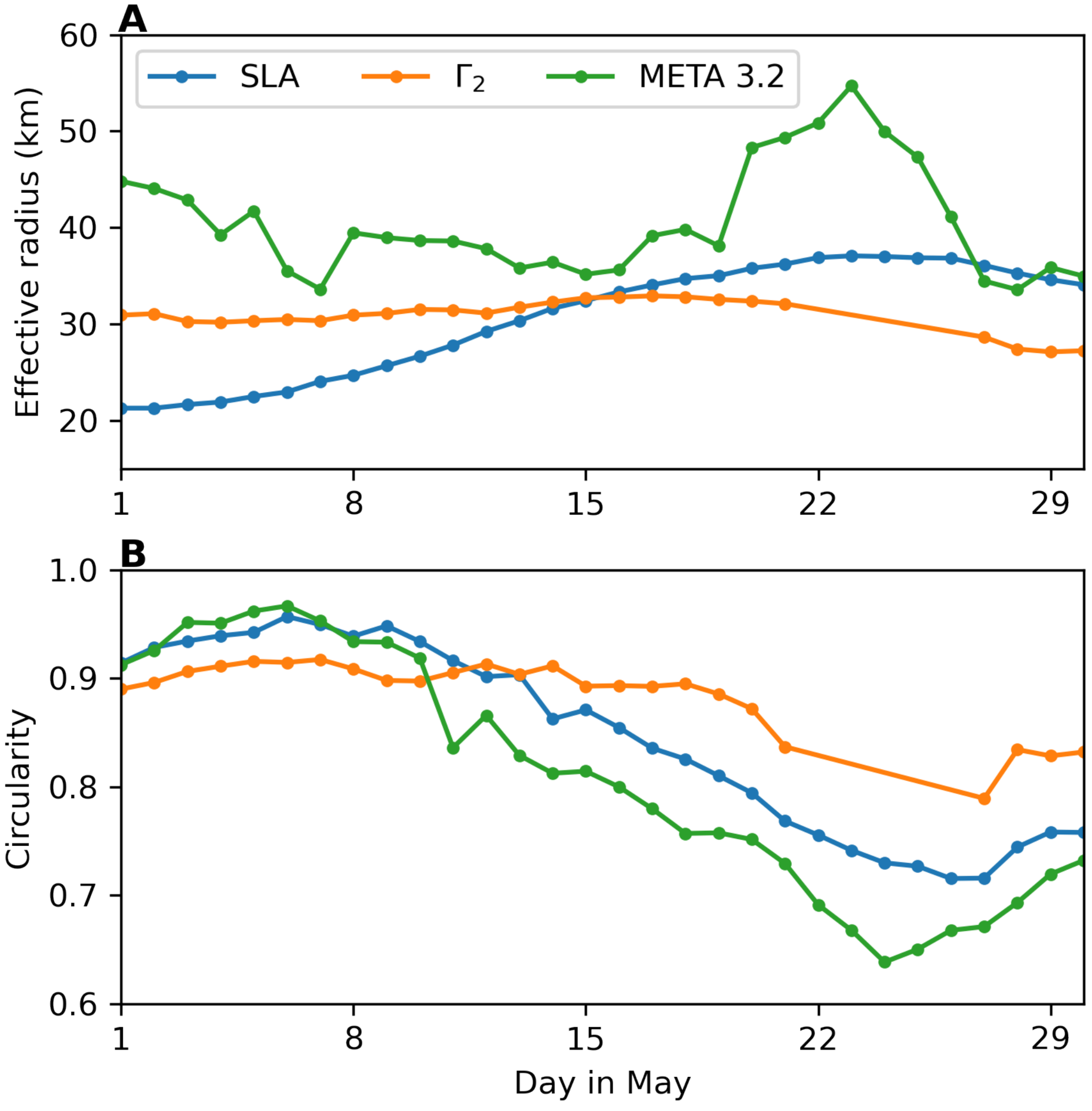
A
B
SLA
Γ2
META 3.2
Effective radius (km)
Circularity
Day in May
60
50
40
30
20
1.0
0.9
0.8
0.7
0.6
1
8
15
22
29